Self-assembled Metal Organic Framework Microflowers as Polysulfides Immobilizers for Lithium Sulfur Batteries

by

Xiaoyuan Dou

A thesis
presented to the University of Waterloo
in fulfilment of the
thesis requirement for the degree of
Master of Applied Science
in
Chemical Engineering - Nanotechnology

Waterloo, Ontario, Canada, 2019

Author’s Declaration

I hereby declare that I am the sole author of this thesis. This is a true copy of the thesis, including any required final revisions, as accepted by my examiners.

I understand that my thesis may be made electronically available to the public.

Abstract

Despite the commercial success of lithium ion batteries in portable electronics, the pursuit of more powerful battery technology has never stopped to meet the rapid development of extended applications such as electrical vehicles and grid-scale energy storage. Under such circumstances, lithium sulfur (Li-S) batteries are gain increasing attentions due to their intriguingly high theoretical energy density (2600Wh kg^{-1}) and good cost effectiveness. Unfortunately, the state-of-the-art Li-S batteries are still suffering from two major issues that greatly hinder their commercial applications. Firstly, lithium polysulfides, as the intermediate products during battery cycling, can readily dissolve into the electrolyte and freely migrate between the anode and cathode region. This behavior is known as the 'shuttling effect' which greatly diminishes the battery capacity, induces side reactions, and increases the overall inner resistance. Secondly, both sulfur and its lithiation product lithium sulfide are insulators. The poor electron and ion transfers in cathode cause high electrochemical polarization especially at high current density, leading to the insufficient utilization of active materials.

To overcome these challenges, one valid solution lies in the construction of porous, conductive and sulfur-adsorptive cathode structure. Extensive sulfur host materials such as various carbonaceous materials, polar inorganics and their composites, have been developed and reported highly effective in promoting sulfur electrochemical reactions as well as confining active materials against the polysulfide shuttling. Beyond the cathode strategy, rational interlayer designs between cathode and separator have been revealed with great promise in further regulating the shuttling behaviors for stable sulfur electrochemistry. Well-selected interlayer materials are expected to establish a multi-functional barrier against the permeation of polysulfides upon battery operation, which is compatible and collaborative to the cathode constructions for strong enhancement of sulfur utilization and suppression of shuttle effect.

In this thesis, a unique flower-like metal organic framework (ZnHMT) is synthesized by a

facile and efficient method. The obtained ZnHMT microflowers were employed for the construction of a multifunctional interlayer towards improved Li-S batteries. Through synthetic optimization, uniform ZnHMT microflowers can be obtained through the fast self-assembly of ultrathin 2D nanosheets within a few minutes under ambient temperature. When implemented as interlayer in Li-S configuration, the as-developed ZnHMT microflowers demonstrate a strong affinity with polysulfides through Lewis acid-base interaction, which effectively confines sulfur species within the cathode section, leading to a significant inhibition on polysulfide shuttling. Moreover, the flower-like assembly architecture not only exposes sufficient absorption sites for sulfur immobilization, but also afford a facile electrolyte infiltration and ion transfer, thus contributing to a fast and durable sulfur electrochemistry.

Consequently, Li-S batteries based on the ZnHMT functional separators and simple carbon-based cathodes achieved an excellent cycling stability with a low capacity decay rate for 800 cycles under 1C, superb rate performance up to 5 C, and high areal capacity at raised sulfur loading of 4.5 mg cm^{-2}. These results confirm the great capability of the as-developed ZnHMT interlayer in boosting the battery performance, which not only offers an easy access to high-performance Li-S batteries but could also enlighten the material designs in other related energy storage and conversion fields.

Acknowledgements

The work reported here was financially supported by the University of Waterloo.

The author would like to thank Dr. Zhongwei Chen and Dr. Aiping Yu for their tremendous guidance and help in the Master's study. Special thanks to Dr. Gaoran Li, Dr. Fei Lu, and Dr. Wenyao Zhang who working closely with the author and offering suggestion, direction, and assistance.

Sincerely thanks to the author's colleagues including, Yue Niu, Ruohan Jiang, Yu Pei, Ruidi Liu, Yanfei Zhu, Yun Bai, Rui Lin Liang, Maiwen Zhang, Yaping Deng, Yijiang, Wenwen Liu, Yan Liu, Meiling Xiao, Jianbing Zhu, Jing Zhang, Pan Xu, Jiahua Ou, Kiyoumars Zarshenas, Sahar Hemmati and many other friends for their help and support.

I would also like to thank my parents and beloved girlfriend for their continuous love and support during my two-year oversea study.

Moreover, I would like to acknowledge support from my reviewers, including Professor Zhongwei Chen, Professor Eric Croiset, and Professor Jeff Gostick.

Table of Contents

List of Figures

List of Abbreviations

Abbreviations	Intended Word/ Phrases
Li-S batteries	Lithium sulfur batteries
MOF	Metal Organic Framework
SEM	Scanning Electron Microscopy
TEM	Transmission Electron Microscopy
EDS	Energy Dispersive Spectroscopy
XPS	X-ray Photoelectron Spectroscopy
XRD	X-ray Diffraction
TGA	Thermogravimetry Analysis
EIS	Electrochemical Impedance Spectroscopy
CV	Cyclic Voltammetry
$Zn(NO_3)_2 \cdot 6H_2O$	zinc nitrate hexahydrate
HMT	hexamethylenetetramine
FTIR	Fourier-transform infrared spectroscopy
BET	Brunner-Emmet-Teller
UV-vis	Ultraviolet-visible
THF	Tetrahydrofuran
SP	Super P carbon
PVDF	Polyvinylidene fluoride
NMP	N-Methyl-2-pyrrolidone
PP	Polypropylene

1. Introduction

Coordinated development of economy, energy, and environment is an important prerequisite for achieving global sustainable goals. However, with the boost of human population, the demand for energy is rapidly increasing while the traditional fossil fuels are about to deplete, leading human society into energy crisis. The unreasonable development of natural resources since the industrial revolution has caused a series of challenges, including environmental pollution, climate change, and ecological deterioration. The latest BP Statistical Review of World Energy 2019[1] states that the current global energy consumption and carbon dioxide emissions is growing at the fastest speed seen for years, which is behind the accelerated transition envisaged by the Paris climate goals. A sharp increase was witnessed for the consumption of multiple traditional energy resources (Figure 1a), many of which grew more strongly than their recent historical averages. It is still a critical challenge to transform the current energy consumption pattern towards cleaner and more sustainable fuels.

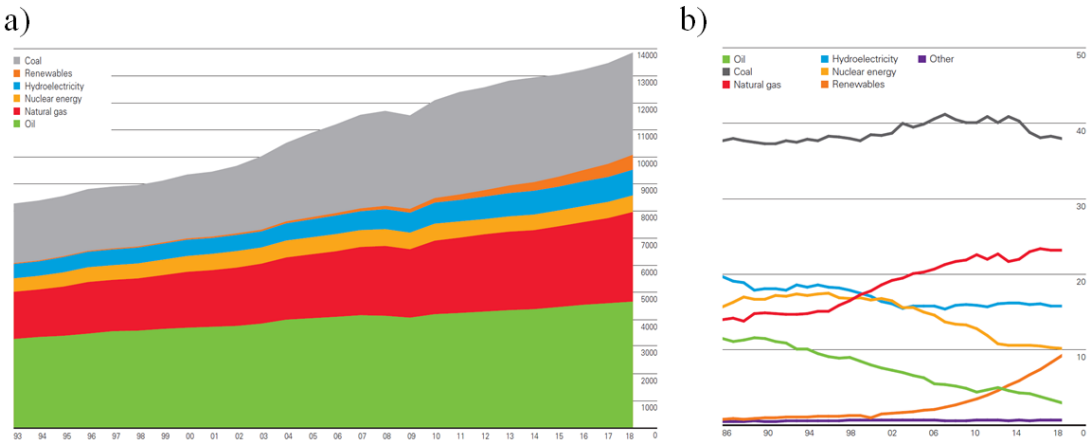

Figure 1 a) Annual world consumption of different energy sources (million tonnes oil equivalent), b) Percentages of the different energy sources for electricity generation[1]

As the world continued to electrify, power demand increased even more significantly than overall energy demand. This shift towards greater electrification can play an important part in the energy transition only if it is accompanied by a decarbonization of the power sectors. Motivated by this point and to relief the pressure of coals for electricity generation (Figure 1b), design and development of high-efficiency energy storage and conversion devices has drawn widespread attention from both basic research and industry applications. Various novel electrochemical devices have been intensely investigated, including rechargeable batteries[2], fuel cells[3], and supercapacitors[4]. Among them, lithium ion batteries are no doubt the most successful battery type in the 21st century. Due to their high energy and power density, lithium ion batteries have dominated the major battery market on applications such as portable electronics and electric vehicles. However, as the lithium ion batteries are about to meet their theoretical capacity limit, other novel batteries, such as lithium sulfur batteries[5] and lithium oxide batteries[6], starts to gain more and more attention from both the academia and industry.

1.1. Lithium Ion Batteries

1.1.1. History and Background

Lithium ion batteries are no doubt the most successful battery type in the 21st century. Due

to their high energy and power density, lithium ion batteries have dominated the major battery market on applications such as portable electronics and electric vehicles. The predecessor for lithium ion batteries are lithium metal batteries. Unfortunately, during the repeat stripping and plating of lithium, lithium dendrites tend to continuously grow on the surface of the lithium anode due to the uneven deposition of lithium ions[7]. The uncontrolled growth of lithium dendrites not only consumes electrolyte but can also pierce through the separator, causing short circuit or even explosion. Due to this intractable problem, the research of lithium secondary batteries stagnated for a long time.

In 1980, Armand et al.[8] proposed an embedded mechanism by replacing the lithium metal with graphite to avoid the lithium dendrites problem. Based on this breakthrough, the so-called 'rocking chair' batteries opened the prelude of lithium-ion battery research. In the early 1990s, Sony Corporation of Japan took the lead in mass production of lithium-ion batteries, marking the entrance of lithium-ion batteries from laboratory to commercial market. Lithium-ion batteries have attracted great interest from both industry and academia in the past two decades due to their superior advantages over conventional secondary batteries like lead-acid batteries and alkaline batteries. A large amount of human and financial resources has been invested in the development of lithium-ion batteries, resulting in the rapid development of lithium-ion batteries. Lithium-ion batteries have a variety of appearances, including columnar batteries, button batteries, block batteries, and soft pack batteries. Regardless of the shape, lithium-ion batteries all consist with a cathode (aluminum current collector + positive electrode material), an anode (copper current collector + negative electrode material), an electrolyte, a separator, and a stainless-steel

battery shell.

1.1.2. Mechanism for Lithium Ion Batteries

To explain the working principle of lithium ion batteries, the most common lithium-ion battery using lithium cobalt oxide as the cathode and graphite as the anode is selected as an example. During the charging process, Li ions move out from the cathode, migrate through the electrolyte, and then embed into the lattice of graphite. At the same time, Co^{3+} in the cathode is oxidized to Co^{4+} while electrons are released to the anode through an external circuit. During the discharge process, Li ions leave the anode and insert back into the cathode. At the same time, the electrons released by the anode are transferred into the cathode through the external circuit to reduce Co^{4+} into Co^{3+}. The above process is illustrated in Figure 2. During repeating charge and discharge process, Li ions shuttle back and forth between the cathode and anode, which is similar to a rocking chair. Hence, lithium ion batteries are also named as "rocking chair" batteries.

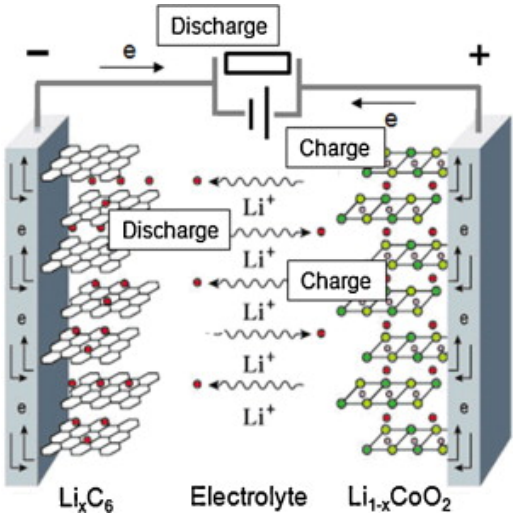

Figure 2 Scheme illustration for the mechanism of lithium ion batteries based on

intercalation mechanism[9]

In a typical lithium-ion battery, the reactions of the cathode and anode are as follows:

Cathode: $LiCoO_2 \leftrightarrow Li_{1-x}CoO_2 + xLi^+ + xe^-$

Anode: $C_y + xLi^+ + xe^- \leftrightarrow C_yLi_x$

Overall: $LiCoO_2 + C_y \leftrightarrow Li_{1-x}CoO_2 + C_yLi_x$

1.1.3. Electrode Materials for Lithium Ion Batteries

The capacity of the lithium-ion battery mainly depends on the number of Li^+ that the cathode and anode materials can provide during electrochemical reactions. In addition, the lattice structure stability of electrode materials also plays an important role to maintain the capacity of lithium ion batteries during cycling. Therefore, the most challenging topic for lithium ion batteries research is the development of electrode materials. The cathode materials of lithium ion batteries mainly include $LiCoO_2$ and $LiNiO_2$ with layer structure, $LiMnO_2$ with spinel structure, and novel ternary materials such as $LiNiMnCoO_2$. Up to now, the most commonly used cathode material in lithium ion batteries is $LiCoO_2$, first proposed by Professor. Goodenough. $LiCoO_2$[9] exhibits a theoretical capacity of 274 $mAhg^{-1}$, but only 140 $mAhg^{-1}$ of the capacity can be recognized in the practical applications. This phenomenon seriously restricts the overall performance of lithium ion batteries. $LiNiO_2$[10] possesses a similar structure and practical capacity (190-210 $mAhg^{-1}$) comparing to $LiCoO_2$. However, pure phase $LiNiO_2$ is hard to synthesis and require crucial conditions, which greatly restricts their commercialization. The spinel structure of $LiMnO_2$[11] is low-

cost and has a relatively good rate performance, but its cycle stability and high-temperature stability demands further improvement. In order to combine the advantages of the above three materials, $LiNiMnCoO_2$[12], a composite containing nickel, cobalt, and manganese, has been developed, falling into the category of ternary cathode materials. By adjusting the ratio of nickel, cobalt and manganese, the performance of the ternary cathode material can be optimized, which makes it a hot cathode material recently.

Compared with the cathode materials, the anode materials in lithium ion batteries has more diversity. Depending on the mechanism to storage lithium ions, the anode materials can be separated into several types. The first type is based on the intercalation mechanism as we just discussed above. A typical example is graphite which has small volume change and stable cycle performance during intercalation and deintercalation process. However, its actual capacity makes graphite hard to meet the demand of high energy density lithium ion batteries. The second type is based on the alloy de-alloy mechanism, in which lithium ions can form alloys with the anode materials. Examples include tin-based[13] and silicon-based materials[14]. The capacity of this type materials is much higher comparing to graphite. Unfortunately, during the rapid alloy de-alloy process, this type materials will suffer a huge volume variation, which can cause pulverization and fast capacity decay.

1.1.4. Challenges for Lithium Ion Batteries

Even though their outstanding cycling and rate performance has made lithium ion batteries superior than other kinds of secondary batteries in the past twenty years, lithium ion

batteries still face challenges. As the intercalation sites for lithium ions are limited by the inner property of electrode materials, lithium ion batteries based on the intercalation mechanism cannot deliver very high capacity. The energy density of the commercial lithium ion batteries ($LiCoO_2$/C) is only 387 $WhKg^{-1}$. Besides, the current price of cobalt is at the highest since 2008 even if the cobalt production rose by 13.9% worldwide[1]. This clearly will increase the production cost of lithium ion batteries in the near future. Under such circumstance, next-generation secondary batteries, such as lithium-sulfur batteries, lithium-air batteries, have drawn widespread attention and been considered as one of the most prospective candidates for the next generation high energy storage devices.

1.2. Lithium Sulfur Batteries

1.2.1. History and Background

The discovery of lithium sulfur (Li-S) batteries was reported as early as 1960s. Whereas, due to more stable performance of lithium ion batteries, research on Li-S batteries had stopped in late 20^{th} century. After 10 years, the rapid development of portable electronic devices is placing a more and more eager demand on the energy density of batteries. As the capacity of lithium ion batteries are about to approach their theoretical capacity, Li-S batteries, which own much higher theoretical energy density, are back to the game and currently under intensive investigation among the world. The theoretical energy density for Li-S batteries is about 2600 $Whkg^{-1}$ when applying lithium as anode and sulfur as cathode[15].

This value is more than six times larger than that of the current lithium ion batteries. Comparing to $LiCoO_2$, sulfur has abundant reserves and low toxicity, which can restrain production cost and environmental pollution at the same time.

1.2.2. Components and Working Principle for Lithium Sulfur Batteries

Lithium sulfur batteries, consisting a similar configuration with lithium ion batteries, use pure lithium metal as anodes and sulfur as cathodes (Figure 3). Due to the insolation nature of sulfur, carbon-based hosts for sulfur are required in order to permit electrons transportation and electrolyte permeation. Polymeric binders are also induced to maintain the integrity of sulfur cathodes during cycling. The electrolyte in Li-S batteries are predominately the mixture of dimethoxymethane (DME) and 1,3-dioxolane (DOL) (1:1 in volume ratio) with 1M bis(trifluoromethane) sulfonimide lithium salt (LiTFSI). Comparing to the well-known carbonate-based electrolytes in lithium ion batteries, ether-based electrolyte can form a more stable solid electrolyte interphase (SEI) with lithium anodes and suppress the formation of lithium dendrites[16]. Also, carbonate-based electrolytes can react with the intermediate products[17], polysulfides, during the cycling of Li-S batteries, causing irreversible capacity decay.

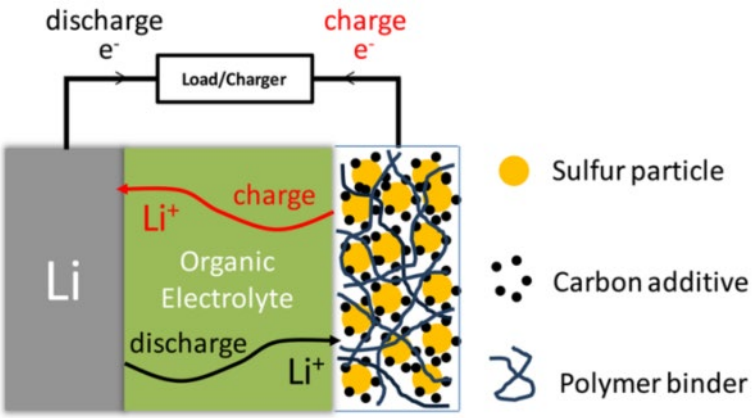

Figure 3 Scheme illustration of a lithium sulfur battery[5]

During the discharge process of Li-S batteries, lithium metal will lose electrons and be oxidized into lithium ions. The electrons and lithium ions will transport through the external circuit and internal electrolyte separately and reach the sulfur cathode. Sulfur will then be reduced to lithium sulfides. During charging, a reversed reaction will happen, in which lithium sulfides will be oxidized back to sulfur and lithium ions will be reduced on the surface of lithium anode. The cathode, anode, and overall redox reaction equations are listed as below.

$$\text{Positive/ Cathode: } S + 2Li^+ + 2e^- \leftrightarrow Li_2S$$

$$\text{Negative/ Anode: } 2Li \leftrightarrow 2Li^+ + 2e^-$$

$$\text{Overall Reaction: } 2Li + S \leftrightarrow Li_2S$$

Whereas, the actual redox reactions happened inside a Li-S battery is much more complicated than the above equations. The transformation between sulfur to lithium sulfides involves several stage reactions with the formation of polysulfides and phase change, as is depicted in Figure 4. Taking the discharge process as illustration, solid sulfur

will be first reduced to long chain solid state polysulfides (Li_2S_x, x= 4~8), corresponding to the first discharge plateau at 2.1-2.4V in the discharge curve. The theoretical capacity for this plateau is 418 $mAhg^{-1}$. The final product in the first discharge process, Li_2S_4, is highly soluble in ether electrolyte and possess high reaction activity. Thus, Li_2S_4 will be subsequently oxidized to lithium sulfides (Li_2S_2 and Li_2S) which is insoluble in electrolyte and non-conductive. This conversion corresponds to the second discharge plateau happening at 2.1V and can deliver a theoretical capacity of 1257 $mAhg^{-1}$. Therefore, the theoretical capacity for sulfur can be up to 1675 $mAhg^{-1}$ which is much higher than that of the current commercial cathode materials in lithium ion batteries.

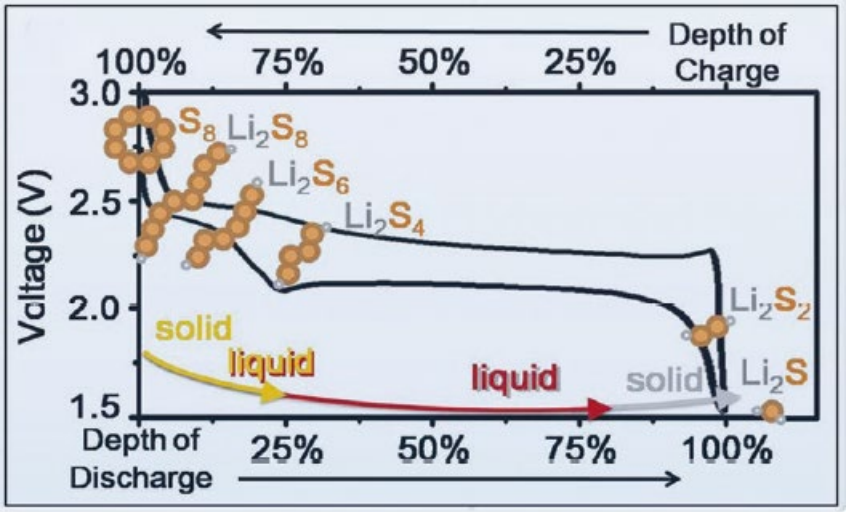

Figure 4 The discharge and charge curve for Li-S batteries and the corresponding reaction stages[18]

1.2.3. Challenges for Lithium Sulfur Batteries

Despite their high energy density and low cost, Li-S batteries still suffer from several problems, which greatly diminish the performance of batteries and withhold their

commercialization progress. The following paragraphs are dedicated to elaborating these challenges.

The first issue is the insulation nature of sulfur and lithium sulfide (Li_2S_2 and Li_2S). The conductivity of sulfur and Li_2S is as low as 10^{-30} and 10^{-14} S cm^{-2}, respectively. Due to this fact, the sulfur redox reactions, especially during the solid to solid conversion at first discharge stage, are sluggish, causing low utilization of sulfur. Moreover, the discharge end products, Li_2S_2 and Li_2S, tend to accumulate on the surface of sulfur cathodes during cycling, which can prohibit sulfur from accessing electrons and lithium ions. As a result, the inner resistance of lithium sulfur batteries will keep increasing and a fast capacity decay will be observed. To overcome the above disadvantages, carbon-based materials and binders are required to increase the electron conductivity between current collectors and active materials. In 2009, Nazar et al.[19] invented a melt-diffusion method to increase the contact area between the insulated sulfur and the high porous carbon-based material. This method greatly improves the utilization rate for sulfur and is now the most commonly used method for the synthesis of sulfur cathodes.

The second challenge for Li-S batteries is the volume change of sulfur cathodes. Sulfur possesses a much higher density (2.07 g cm^{-3}) than that of lithium sulfide (1.66 g cm^{-3}). Consequently, the reversible conversion during charge and discharge will cause severe volume change in cathodes. The volume change can destruct the electrode integrity and create gaps between the active materials and the conductive agents. Without access to electrons, the isolated sulfur will increase the cell impedance and can no longer contribute

any capacity. Fortunately, due to the invention of the melt-diffusion method, most of the current carbon-based sulfur hosts are designed to own high porosity with wide pore size distribution[20]. As a result, the volume change of sulfur can be greatly buffered. However, it should be mentioned that the introduction of high void sulfur hosts will inevitably reduce the volumetric and gravimetric energy density of lithium sulfur batteries.

The third problem for Li-S batteries, which is the most fatal one, is the polysulfides shuttling effect. As we have just discussed in section 1.2.2, polysulfides are highly soluble in electrolyte, which endows them with high mobility and reactive property. This feature accelerates the redox kinetics and favors for the sulfur conversion rate. However, thanks to this property, polysulfides can also easily diffuse from the cathode region to anode region due to the large pores on separators and concentration gradient. This triggers the 'self-discharge' behavior of Li-S batteries (Figure 5a). The migrated polysulfides can react with lithium anode through direct chemical reactions and deposit as insulated lithium sulfide on the surface of lithium anode. This causes loss of active material, severe corrosion on lithium anodes, and fast decay of battery capacity. What's more, during the charging process, the long chain polysulfides floating into the anode region can be directly reduced to short chain polysulfides. These short chain polysulfides will move back to cathode area due to electric field and be reduced to long chain polysulfides. This phenomenon is known as the polysulfides 'shuttling effect'[21] (Figure 5b). Polysulfides will continue to move back and forth between the cathode and anode, resulting in infinite charging status and low Columbic efficiency.

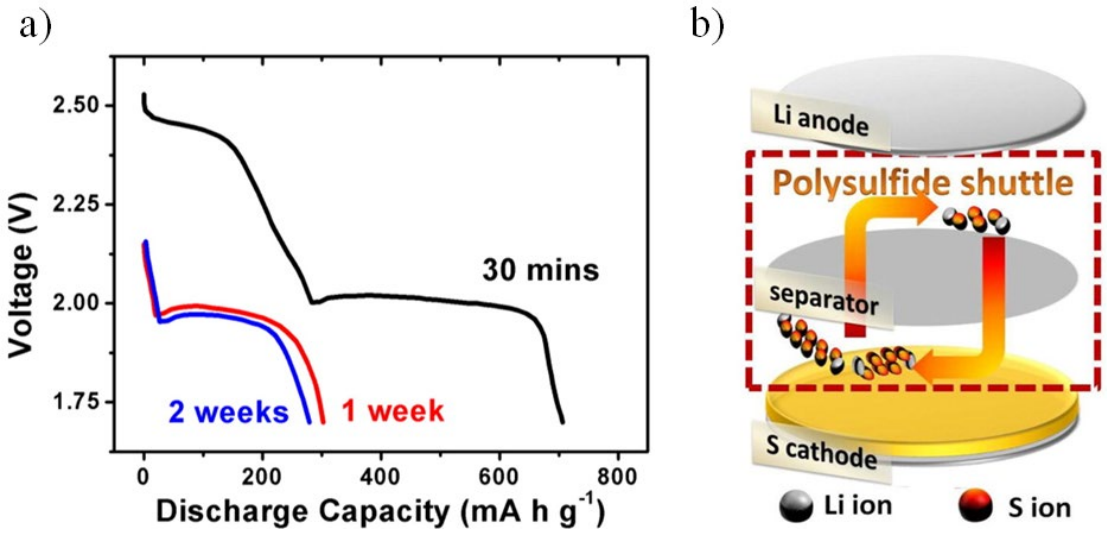

Figure 5 a) The discharge curves of Li-S batteries with conventional sulfur cathodes after different rest time, b) Scheme illustration for the shuttling effect in a Li-S battery[5]

1.2.4. Research Progress for Li-S batteries

As what we have just talked about, the insulating sulfur and polysulfides relocation are the major technical challenges for Li-S batteries. To tackle with these, various modifications on sulfur cathodes and separators have been reported by many researchers, which all aim to (1) prohibit the migration of polysulfides and (2) improve the overall electrical conductivity to achieve a higher utilization of sulfur. In this section, a short summary regarding to the current research progress in Li-S batteries will be presented.

1.2.4.1. High Performance Sulfur Host Materials

The solution dealing with the insulating sulfur is quite straightforward, which is the addition of conductive carbon. Thanks to the fast development of nanomaterials,

engineered porous carbon materials with high conductivity and narrow pore size[22-24] becomes promising candidates as sulfur host materials. The interconnected carbon network can shorten the transportation pathway for electrons while the intimate connection between sulfur and carbon can greatly promote the sulfur utilization rate. In addition, high surface area porous carbon materials ensure a sufficient sulfur loading for the cathodes. Gao et al.[25] reported the synthesis of carbon spheres with micropores. The narrow micropores can greatly restrain the movement of polysulfides during cycling. Based on the same principle, many other carbon materials, including hierarchical porous carbon[26-27], hollow carbon spheres[28], carbon nanotubes[29-30], and graphene[31-32], have been applied as sulfur host materials.

1.2.4.2. Functional Separators and Interlayers for Li-S Batteries

In addition to the wide investigation for cathode materials, research on the functional separators and interlayers for Li-S batteries also gains many attentions. Various polysulfides-inhibited materials reported for the cathode materials in the last paragraph also have been induced onto the routine separators to upgrade the traditional configuration of Li-S batteries.

At the early stage, carbon-based materials possess minor interaction with polysulfides were investigated. Manthiram et al.[33] demonstrated the direct coating of Super P carbon onto the PP separators. The robust carbon-coated separators exhibit strong physical blocking ability

for polysulfides. However, a thick coating layer is required for 0D materials like Super P. Because of this, 1D and 2D materials, such as carbon nanotubes[34] and graphene derivates[35], are also reported due to their anisotropic shape and longer diffusion pathway for polysulfides. With the help of single wall carbon nanotubes-modified separators, Li-S cells exhibit a high reversible capacity with a capacity decay rate of 0.18% per cycle. The mass loading for this functional separator is merely 0.13 mg cm^{-2}.

Due to the non-polar nature for carbon materials, endeavor to introduce heteroatoms or polar groups into the carbon matrix have also been made in order to increase the interaction force with polysulfides. This type of separators is also known as bi-functional separators since they can both increase the overall electronic conductivity and polysulfide affinity. The introduction of N[36], P[37], S[38], O[39], and B[40] doping into carbon skeletons all displayed positive effect. Giebeler et al.[41] reported a functional separator coated with a N and S codoped mesopores carbon material in Li-S batteries. The cell equipped with this novel separator exhibits better kinetics and higher utilization of sulfur. DFT calculations reveal that the interaction energy of polysulfides with N-doped sites is 1.46eV only if there is sulfur doping nearby. On contrary, the interaction energy for pure N-doped sites is only 0.3eV. Comparing to the heteroatom-doped carbon materials, metal oxide, such as SiO_2[42], ZnO[43], MnO_2[44] and TiO_2[45], owns even higher polysulfides affinity property. An interlayer, which composed of conductive frameworks and ZnO nanowires, was constructed by Zhao et al[43]. The strong attraction between polysulfides and ZnO helps Li-S batteries to deliver a reversible capacity around 800 $mAhg^{-1}$ for 200 cycles with slow capacity decay rate.

1.2.4.3. Metal Organic Frameworks (MOFs) in Li-S batteries

Metal organic frameworks (MOFs), composed by the ordered coordination between metal nods and organic ligands, are a promising type of crystalline materials due to their high surface area and porosity[46]. By varying the types of metal nods and ligands, structures with different coordination pattern, pore size and chemical property can be easily obtained, exhibiting the high diversity in MOF family. As a result, various research topics on MOF materials have been reported in fields such as energy storage[47], separations[48], catalysis[49], and chemical sensors[50]. Especially, the introduction of MOFs into Li-S battery system is becoming an intriguing research area recently[51]. Because of their non-conductive nature, most MOF materials are not suitable to be directly used as sulfur hosts. Instead, they are the perfect candidates as immobilizers to decorate the conventional separators and withhold the negative 'shuttling effect'. The high surface area of MOF materials increases the diffusion pathway for polysulfides while their metal nods can chemically absorb polysulfides through Lewis acid-base interaction. Zhou et al.[52-53] first reported the application of MOF particles in separators modification. The MOF they synthesized owns ordered micropores with narrow pore size of only 9 Å and thereby can functional as an efficient ionic sieve for polysulfides. However, the morphology of MOF immobilizers reported so far in Li-S battery research are predominantly as particles[54-58]. With such morphology, MOF particles can only expose limited chemisorption sites and tend to aggregate easily[55], severely diminishing their polysulfides trapping capability. In order to overcome this problem, some researchers utilized ultrathin 2D MOF nanosheets[59] to modify the conventional separators. Whereas, the complicated synthesis route, harsh

synthesis conditions, and lack of understanding on MOF nanosheets formation mechanism[60-62] offer very few 2D MOF candidates for Li-S batteries.

1.3. Thesis Scope

The insulation nature of sulfur and polysulfides relocation are the two main factors that hinder the development of Li-S batteries. Research on the modification of sulfur cathodes structure and separators are proved to be effective strategies to overcome these challenges. In this thesis, a metal organic framework with hierarchical morphology was fabricated through a fast and facile strategy. Then, it was applied as polysulfides immobilizers onto the conventional separators in Li-S batteries. Both physical and electrical characterization results confirm the strong polysulfides confinement ability of this novel functional separators.

The work of this thesis concentrates on:

a) The fabrication and characterization of self-assembled hierarchical ZnHMT microflowers. A suitable synthesis condition was concluded by investigating various parameters.
b) The development of ZnHMT@PP functional separator and its application in Li-S batteries.

1.4. Organization of Thesis

This thesis is organized in five chapters. Chapter 1 discusses the general background, fundamental concept, limitations, and research progress for lithium ion batteries and lithium sulfur batteries. Chapter 2 elaborates the physical and electrochemical characterization techniques applied in this thesis. Chapter 3 presents the preparation of ZnHMT microflowers, including various characterization results and exploration for optimal fabrication conditions. In Chapter 4, the as-synthesized ZnHMT microflowers are adapted as immobilizers and decorated onto the conventional separators. The results from polysulfide absorption experiment and polysulfide permeation experiment illustrate the strong affinity between polysulfides and ZnHMT microflowers. Various electrochemical measurements results were also provided and discussed in detail. Finally, in chapter 5, a conclusion on this thesis is provided.

2. Characterization Strategies

2.1. Physical Characterization

2.1.1. Scanning Electron Microscopy

Scanning electron microscopy (SEM) is the most popular physical characterization technique for material research. It applies a focused high energy electron beam as probe to scan the surface of specimens and transform the reflected electrons to digital images to depict the morphology. As the wavelength of electrons is much smaller than that of light, SEM can provide higher resolution comparing to that of the light microscopy.

An SEM machine consists of an electron gun, two condenser lenses, one objective lens, one detector system, and a high vacuum chamber (Figure 6). To generate electron beam, two types of electron guns, thermionic emission guns and field emission guns, are commonly used. The first one, typically using tungsten or lanthanum hexaboride as filaments, creates electron beam through heating the filaments under high temperature which can be up to 2800K. For the field emission gun, a strong electric field is applied to the gun and consequently draw electrons off a very sharp tip. The field emission guns can provide higher brightness while be operated at a relatively low temperature (1800K). As the focused electron beam plays as a probe to scan the materials in a SEM, the electron beam with smaller diameter (smaller probe size) creates a higher resolution. However, a delicate balance between the acceleration voltage, probe current, aperture size, and

working distance need to be achieved before getting the optimize resolution. Most modern SEM systems are now equipped with a field emission gun to maintain the brightness while are operated under low acceleration voltage to maintain the spatial resolution.

Because electrons can't be focused or deflected through glass, all the lenses in SEM are electromagnetic lenses and can be controlled by current. Both the condenser and objective lenses decrease the diameter of electron beam to nm scale and direct the electron beam to bombard onto the sample surface. Once the electrons strike a sample, either elastic or inelastic scattering of electrons will happen and be collected as two types of signals. The first one is the secondary electrons (SEs). As the SEs are the inelastic scattering electrons, they possess low energy and originate from the surface of the sample (5-50 nm in depth). As a result, the SEs signal can provide topographical information of the sample. On the other hand, the elastic scattering pattern creates the backscattered electrons (BSEs) signal. This type of signal has higher energy and is sensitive to the element composition of the sample. Elements with higher atomic number will become brighter in the BSEs images.

In this thesis, a Zeiss LEO FESEM 1530 SEM was used to probe the morphology of the ZnHMT microflowers. In addition, it provided the morphology information of the separators and lithium anodes before and after the cycling from PP cells and ZnHMT@PP cells, which explicitly prove that polysulfides can't pass through the ZnHMT@PP separators. Before the test, samples were directly pasted onto the SEM stubs using conductive carbon tapes and sputtered with gold.

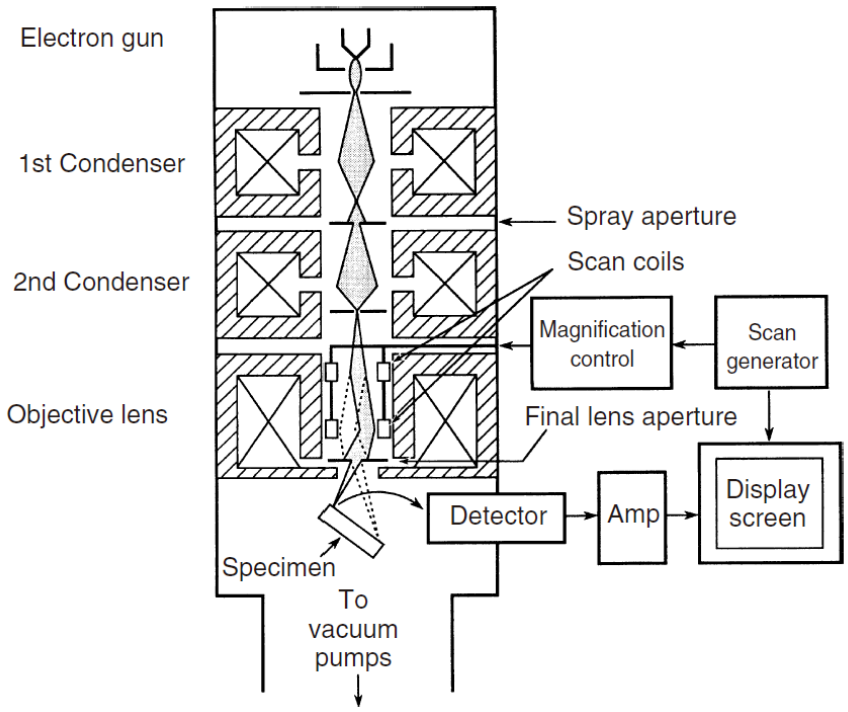

Figure 6 Structure of a scanning probe microscopy[63]

2.1.2. Transmission Electron Microscopy

Transmission Electron Microscopy (TEM) is another powerful physical characterization technique. Comparing to SEM, TEM can offer a much higher magnification (500-1000000×). Consequently, it requires an acceleration voltage up to 200kV and high vacuum level to boost electrons with high energy. With such high voltage, the resolution of TEM can be as low as 0.13nm. TEM possesses a similar structure as SEM, with two condenser lenses, an objective lens, and a projector lens (Figure 7). However, unlike the SEM system, the condenser lenses in a TEM are directly used for the illumination of the specimen and formation of images. As described in its name, a TEM image is obtained by collecting the transmission electrons that pass the specimen. Due to the interaction between the electrons

and specimen's atomic nucleus, electrons in some area will be deflected from their main direction, which will decrease the local intensity of the transmission beam. A thick area in the specimen can prevent a large number of electrons passing, and vice versa. As a result, not only the surface but also the inner morphology of a specimen can be depicted based on the intensity variation of the transmission electron beam.

The TEM images in this thesis were obtained using a Philips CM 10 TEM. To prepare the sample, ZnHMT powder was first sonicated in anhydrous ethanol and then drop onto a carbon coated copper mesh. In this work, TEM is applied to exhibit the inner structure of the ZnHMT microflower and the morphology of single ZnHMT nanosheet. TEM results illustrated that the ZnHMT microflowers possessed more absorption sites comparing to that of the traditional bulk structure.

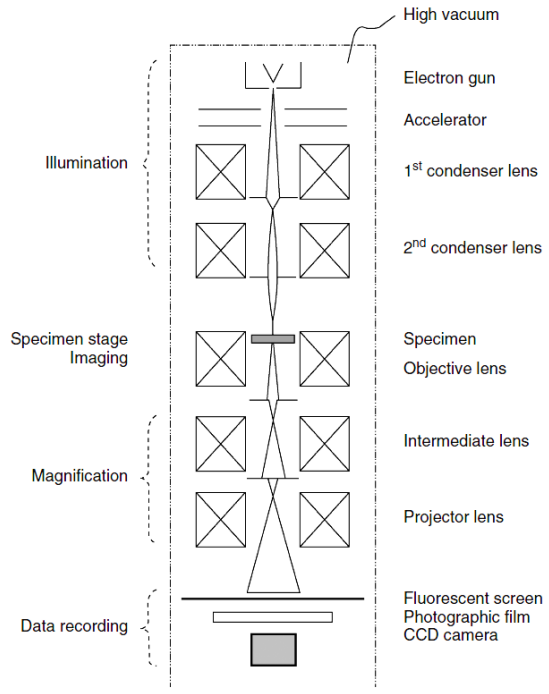

Figure 7 The structure of a transmission electron microscopy[63]

2.1.3. Energy Dispersive Spectroscopy

Energy dispersive spectroscopy (EDS) is a very common and powerful analyzer for electron microscopes (EMs). It can examine the element composition in specimens through detecting the emitted characteristic X-ray energy from samples. In EMs, EDS applies the electron beam from the electron guns, rather than inducing a primary X-ray, to trigger the ignition of an electron from the inner orbit of an atom. The knocked-out electron will leave a vacancy on the orbit and make the atom unstable. In order to be back to stable status, another electron from a higher energy orbit will jump into this inner orbit and emit X-ray photons (Figure 8). As the energy difference between different orbits for each element is a unique and constant value, the energy of this characteristic X-ray can be matched with specific elements. Based on the type of the vacancy orbits, the characteristic X-ray is denoted as K, L, M. In addition, Greek letters (α, β, γ) are used to represent the intensity of the X-ray, where α has the highest intensity. There are two mode for the EDS. The first one is stationary mode, in which the probe will keep collecting the X-ray signal in one location and the intensity of the signal is directly decided by the dwell time. The result is often presented as a spectrum using energy (KeV) as x axis. Therefore, peaks at desired positions can prove the presence of corresponding elements. The second mode is the scanning mode, in which the probe will scan the selected area and collect the radiate X-ray. These X-ray signals will be corresponded to the electron image and together form the element mapping result. The element mapping can visually demonstrate the distribution of elements.

In this thesis, the scanning mode of EDS was conducted to detect the element distribution

on ZnHMT microflowers and demonstrate that ZnHMT microflowers were uniformly distributed on the ZnHMT@PP separator. The stationary mode was performed on the anode side of ZnHMT@PP separators and PP separators after battery cycling, in order to confirm that PP separators had much higher sulfur content. Results from both characterizations indicate that the ZnHMT microflowers on ZnHMT@PP separators can greatly retard the migration of polysulfides.

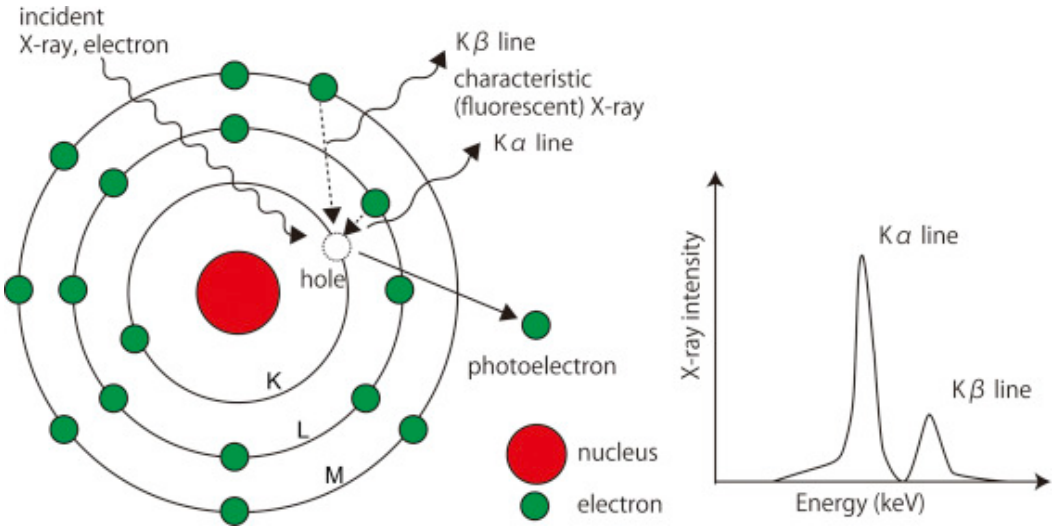

Figure 8 The mechanism for energy dispersive spectroscopy[64]

2.1.4. X-ray Photoelectron Spectroscopy

X-ray photoelectron spectroscopy (XPS) is a technique for surface chemical analysis through collecting the excited electrons from the samples based on the photoelectric effect[65]. Comparing to the high energy characteristic X-ray in EDS, the photoelectrons for XPS characterization can only escape from the uppermost surface (~10nm) of the samples due to their low energy, making XPS a powerful characterization technique for chemical environment analysis. Like electron microscopy, XPS requires high vacuum, which can

prevent photoelectrons being deflected by air molecules and keep the surface of sample from contamination. Under the radiation of primary X-ray, electrons from inner orbit of an atom will fully absorb the induced X-ray energy (hv), overcome their binding energy with the nucleus, and excite out with a kinetic energy (KE). As the energy of this induced X-ray is known and we can measure the kinetic energy of electrons, the binding energy for electrons from different chemical environments can be calculated, based on Equation 1. Matching these results with standard references, we can figure out the composition and chemical environment in specimens. What's more, combining with the ion gun in the XPS system, a depth XPS profile can also be developed.

$$E_B = h\nu - KE \quad \text{(Equation 1)}$$

In this thesis, XPS was performed to find out the chemical environment of Li_2S_6, ZnHMT, and ZnHMT@Li_2S_6. The chemical shift between Li_2S_6 and ZnHMT@Li_2S_6 implies ZnHMT can strongly attract polysulfides through chemical interaction. These results are in consistent with the absorption experiment and provide detailed evidence from the molecular level.

2.1.5. X-ray Diffraction

X-ray diffraction is a well-known method for characterizing the crystal structure of samples. Samples with different crystal patterns can be distinguished by X-ray diffraction even if they have the same composition. X-rays are waves but with much shorter wavelength ($\lambda \approx 0.1$nm) comparing to visible light. Therefore, two identical waves can interact with each other if they travel in the same direction. A constructive interference occurs when the phase

difference is nλ. A fully destructive interaction happens when the phase difference is nλ/2. Monochromatic X-ray can be reflected by the crystallographic plane in a crystal as is shown in Figure 9. A constructive interference can happen only if the incident angle (θ) and X-ray wavelength satisfy the Bragg's Law in Equation 2. Then, the spacing between atomic planes can be obtained and used to determine the crystal structure of materials. In this work, x-ray diffraction was applied to verify the crystal structure of ZnHMT microflowers. The result is in consistent with previous reports even though a unique morphology is accomplished in this work.

$$n\lambda=2d\sin\theta \qquad \text{(Equation 2)}$$

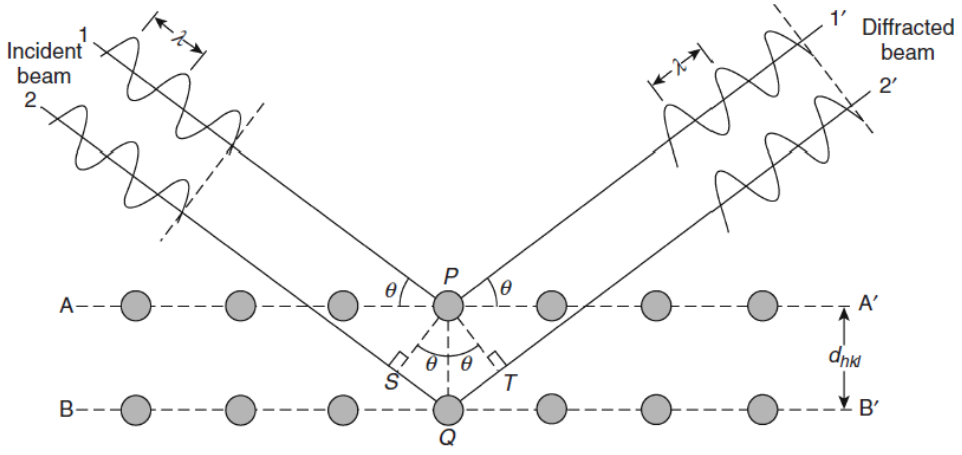

Figure 9 Scheme illustration for Bragg's diffraction[63]

2.1.6. Ultraviolet-Visible Spectroscopy

Ultraviolet-visible (UV-vis) spectroscopy is a technique that measures the absorption of ultraviolet (from 190 to 400nm) and visible light (from 400-800nm) by samples. By utilizing the radiation energy of UV-vis light, electrons in the lower orbits can jump into higher orbits. Through measuring the light intensity that passing through the sample

solution (I) and blank solution (I_0), the absorbance intensity (A) can be calculated based on Equation 3. An UV-vis spectrum, with wavelength as x axis and absorbance intensity as y axis, is often plotted to exhibit the results. As each functional group requires a particular energy to excite electrons, the absorption peaks in UV-vis spectra can qualitatively imply the presence of specific functional groups. In addition, based on the Beer-Lambert Law, the concentration of the sample solutions can be quantitatively obtained through constructing standard calibration graph.

$$A=\boldsymbol{log}_{\mathbf{10}}\frac{\boldsymbol{I_0}}{\boldsymbol{I}} \quad \text{(Equation 3)}$$

In this thesis, UV-vis spectroscopy was performed for Li_2S_6 solutions and ZnHMT@Li_2S_6 solutions during the absorption experiment. Comparing to the results for Li_2S_6 solutions, the characteristic absorption peaks representing the polysulfides disappeared in the results of ZnHMT@Li_2S_6 solution, indicating the strong polysulfide affinity of ZnHMT microflowers.

2.1.7. Thermogravimetry

Thermogravimetry analysis (TGA) is a measurement that tests the mass change of samples under different temperature and atmosphere. The temperature can be a fixed value or increase in a range under desired heating rate, depending on the test goal. By using a highly sensitive microbalance, any minor mass change (±1μg) during the test will be recorded. The result of TGA is often presented as a curve with temperature as x axis and weight percentage as y axis. This curve can offer information such as the decomposition

temperature and mass ratio of different compositions in a mixture. The mass of the testing samples, heating rate, and gas flow rate can considerably impact the TGA curve.

For this work, TGA test was conducted on a TA instrument Q500 in order to determine the sulfur content in the S/SP composite. The sulfur content of S/SP composite is an important parameter as it directly determines the sulfur loading on cathodes and the specific capacity of Li-S cells. During the TG test, as temperature increasing, S will begin to boil at 444.6℃ and sublime easily, leaving SP behind. Therefore, the mass loss percentage of the S/SP composite is the corresponding sulfur content. For the TGA test, the temperature range was chosen from 80 to 500℃ at the heating rate of 5℃ min^{-1} under nitrogen gas.

2.1.8. Brunauer-Emmett-Teller Specific Surface Area Analysis

Brunauer-Emmett-Teller (BET) analysis is widely used to evaluate the specific surface area and pore size distribution of samples. In battery research, materials with high surface area and wide pore size distribution favors for the permeation of electrolyte and fast transportation of ions and electrons, which can improve the kinetics of electrochemical reactions and battery performance. Therefore, BET result is an important parameter for energy storage research. The specific surface area is obtained by the adsorption of an inert gas on the surface of samples and calculated by the amount of gas molecules assuming a monolayer adsorption. During the test, a degas process, which require high temperature (200℃) and vacuum, will first be conducted in order to remove any impurity from the sample surface. Then, inert gas (N_2 or Ar) will be induced into the system. To avoid any

chemical adsorption happens, the adsorption/desorption process is performed at the boiling point of liquid nitrogen. Equation 4 are used to determine the specific surface area of samples:

$$\frac{P}{v(P^* - P)} = \frac{1}{v_{\text{mon}}c} + \frac{c-1}{v_{\text{mon}}c}\frac{P}{P^*} \quad \text{(Equation 4)}$$

P is the equilibrium pressure; P^* is the vapor pressure of the adsorbate; v is the volume adsorbed at P; v_{mon} is the value under monolayer adsorption; c is a constant at fixed temperature.

Drawing a plot of $\frac{P}{v(P^*-P)}$ versus $\frac{P}{P^*}$, which is a straight line, can give us the value of v_{mon}. Therefore, the specific surface area (S) of the sample can be calculated based on Equation 5.

$$S = \frac{v_{mon}N_A}{22400\ cm^3mol^{-1}} \cdot \frac{A}{m} \quad \text{(Equation 5)}$$

N_A is the Avogadro constant; A is the cross-sectional area for the gas molecule; m is the sample mass.

2.2. Electrochemical Characterization

2.2.1. Cyclic Voltammetry

Cyclic voltammetry (CV) is a potential technique that are often applied to detect the possible chemical reactions in batteries. Before the CV measurement, we first choose two

terminal voltages, a scan rate, and the number of scan cycle. The terminal voltages are quite similar to the cutoff voltage and the scan rate is essentially the C-rate in the galvanostatic discharge-charge test. During the CV test, the applied voltage will keep scanning back and forth between the terminal voltages at constant scan rate until reaching certain scan cycles. A scan that starts from a high voltage and ends at a low voltage is defined as a cathodic scan while the reverse direction scanning is an anodic scan. (Figure 10)

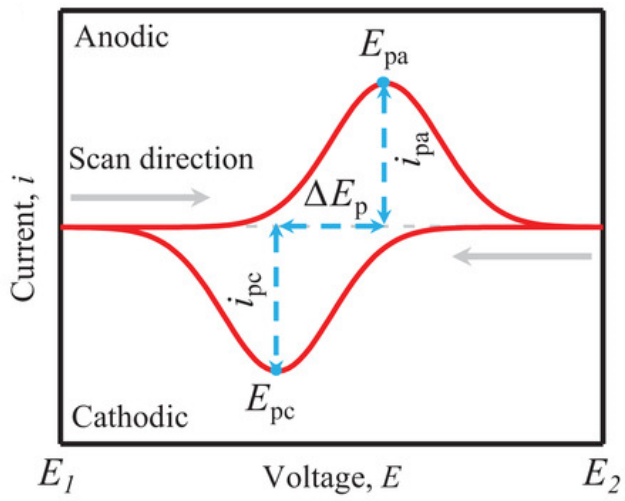

Figure 10 Current versus voltage plot for CV measurement[66]

Electrochemical reactions will happen at specific voltages and generate current. The current or current density is recorded during the test and plotted against scan voltage. Therefore, any peak in the CV diagram represents an electrochemical reaction. In a galvanostatic discharge-charge test, a high C-rate often causes a sluggish reaction kinetics and thereby incomplete redox reactions. To avoid these issues, the scan rate for CV test is typically very slow (from 0.1-10mV s^{-1}), so that all the electrochemical reactions can appear as peaks in CV diagrams. In a CV diagram, the positions of peaks equal to the onset voltage for electrochemical reactions happen while the area of peaks represent the

corresponding capacity for this reaction.

In this work, CV measurement was performed on a Gamry 5000E workstation for PP cells and ZnHMT@PP cells. The voltage range was set between 1.8-2.6V and the scan rate is 0.1mV s^{-1}. A typical peak pattern for Li-S batteries with carbon-based cathodes was found for both cells. More importantly, the CV results implied that ZnHMT@PP separators helped to improve the slow sulfur reaction kinetics and increase the battery capacity, comparing to the conventional PP cells.

2.2.2. Galvanostatic Discharge-Charge Test

Galvanostatic discharge-charge (GDC) test is the most important characterization for battery research, it can provide the voltage variation and capacity of batteries during discharge and charge process. During the test, a constant discharge current will first be applied to the battery until the battery working voltage reaches cut-off voltage. Then, the battery will be charged under the same current until full charged. Multiple parameters, such as current, time, capacity, voltage variation, coulombic efficiency, and cycle numbers, will be recorded and used to evaluate the stability and energy density of the test batteries. C-rate is a jargon to describe the current applied on test batteries. For example, if the current is 1C during the GDC test, fully discharge or charge 1 gram of the active material will take an hour. Therefore, if a Li-S battery has 1 gram of sulfur on its cathode and we want to discharge this battery at 1C, a current equal to 1675mA is required as sulfur has a theoretical specific capacity of 1675mAhg^{-1}. Equally, 0.2C and 5C for this battery would be 335mA

and 8375mA, respectively.

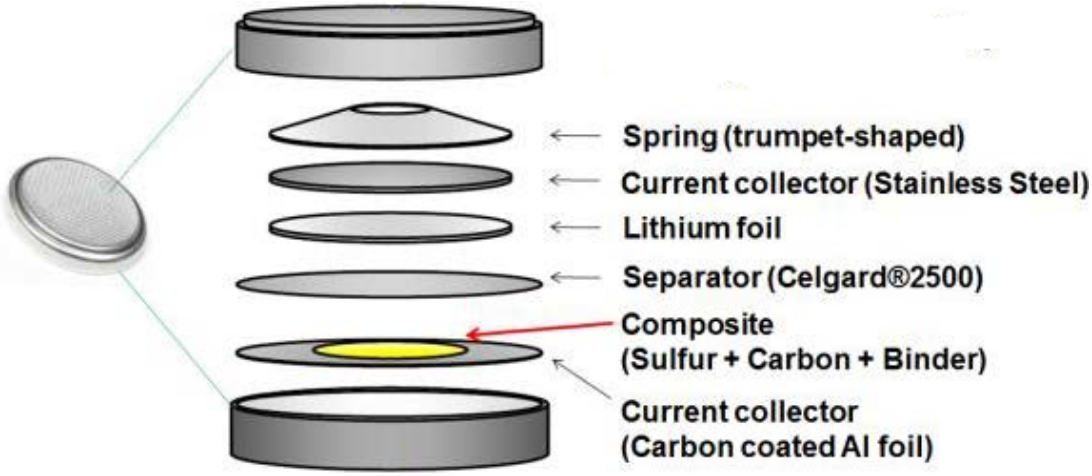

Figure 11 The structure of a 2032 type coin cell[67]

In this thesis, galvanostatic discharge-charge tests were performed on a LAND battery tester to investigate the polysulfide affinity of ZnHMT functional separators. 2032-type coin cells were assembled in a glove box with the concentration of oxygen and water lower than 0.5ppm. The configuration of 2032-type cell is presented in Figure 11.

3. Synthesis of ZnHMT microflowers

3.1. Experimental Methods

At room temperature, 1.061g zinc nitrate hexahydrate ($Zn(NO_3)_2 \cdot 6H_2O$) and 0.25g hexamethylenetetramine (HMT) were dissolved into 15ml and 12.5ml anhydrous ethanol respectively. The molar ratio between $Zn(NO_3)_2 \cdot 6H_2O$ and HMT is 2:1. Then, the $Zn(NO_3)_2 \cdot 6H_2O$ solution was directly poured into the HMT solution. The above mixed solution was aged in a stationary condition for an hour allowing the reaction to complete entirely. After that, the precipitation was collected by vacuum filtration and washed with anhydrous ethanol three times to remove the unreacted reactants. Finally, the as-synthesized white powder was dried in an 80℃ oven for 12 hours.

As a self-assembly process is commonly known to be very sensitive to experiment conditions, the impact of various experiment parameters was also investigated in detail. These parameters include the molar ratio between $Zn(NO_3)_2 \cdot 6H_2O$ and HMT (1:1, 2:1, 4:1), reaction temperature (0, 20, 25, 30, 45℃), reaction time (5 min, 0.5, 1, 12 hours), and water content in solvent(0%, 1%, 10% in volume ratio comparing to ethanol).

3.2. Results and Discussions

Figure 12 illustrates the preparation of ZnHMT microflowers through a fast and facile solution-based reaction. The direct mixing of $Zn(NO_3)_2$ and HMT renders the self-coordination between Zn ions and organic ligands to yield the white ZnHMT precipitate. The successful construction of the metal-organic framework was confirmed by XRD and FTIR measurement. As shown in Figure 13a, the FTIR spectra was witnessed broadened and intensified peaks from HMT to ZnHMT at ~3500 $cm^{-1}$and ~1382.7 cm^{-1}, which is ascribed to the vibration of -OH and $NO3^-$, respectively, indicating the incorporation of hydrophilic $Zn(NO_3)_2$ in the obtained framework[68]. Meanwhile, the peak splitting at ~1250 cm^{-1} assigned to the C-N vibration suggests the networking between Zn ions and ligands. A distinct variation can also be observed in XRD results. In Figure 13b, the XRD pattern of HMT exhibits characteristic peaks at 17.83, 31.14 and 44.62 degrees, corresponding to the (110), (211), and (222) lattice (referring to PDF#39-1843). However, these peaks completely vanish accompanied by the emergence of a group of new peaks for the obtained ZnHMT precipitate, which is consistent with the past literatures. This result further confirms the coordination between metal ion and organic ligand as well as the decent crystallinity of the obtained framework. X-ray photoelectron spectroscopy (XPS) was performed to further investigate the chemical environment of ZnHMT (Figure 13c). In Figure 13d and Figure 13e, the peaks at 286.9 eV and 399.7 eV correspond to the C-N bonding[69], the peak at 407.0 eV can be assigned to the NO_3^- group[70-71], and the strong peak at 1022.3 eV represents the presence of Zn^{2+} ions[72] (Figure 13f).

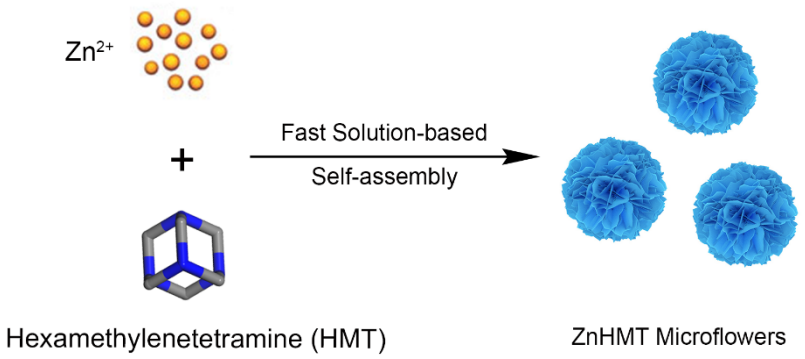

Figure 12 Schematic illustration for the synthesis process of ZnHMT microflowers

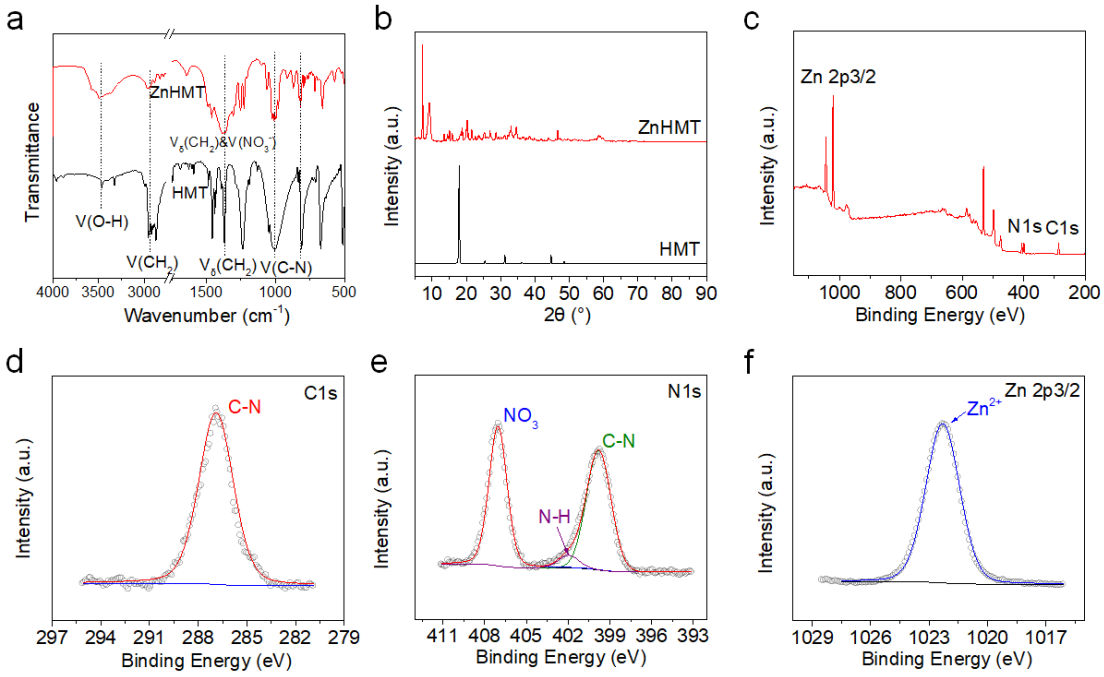

Figure 13 a) FTIR spectra for ZnHMT and pure HMT, b) XRD pattern for ZnHMT and pure HMT, c) XPS survey spectra, d) high resolution C1s, e) N1s, and f) Zn2p3/2 XPS spectra for ZnHMT

Various characterization techniques were conducted to probe the morphology of the ZnHMT microflowers. Figure 14a is the scanning electron microscopy (SEM) image

presenting a group of ZnHMT microflowers. The diameter of the microflowers is around 2-3 μm and each microflower consists of a large amount of 2D ZnHMT nanosheets (Figure 3.3b). In Figure 14c and 14d, the 2D nanosheets are almost transparent under the high energy electron beam of transmission electron microscopy (TEM), indicating its ultrathin thickness. These wrinkled 2D nanosheets, seem to be as flexible as silk, are intertwined with each other and assemble into one microflower. In Figure 14e, the energy-dispersive X-ray spectroscopy (EDS) elemental mappings are in consistent with the SEM structure, indicating the uniform distribution of Zn, N, and C elements and high phase purity. Figure 14f presents the N_2 adsorption/desorption isotherms and the corresponding pore sized distribution of ZnHMT microflowers based on the Barrett-Joyner-Halenda (BJH) calculation and density functional theory (DFT) calculation. The Brunner-Emmet-Teller (BET) specific surface area of ZnHMT microflowers is 15.87 m^2g^{-1} while the pore size distribution implies the hierarchical structure of ZnHMT microflowers.

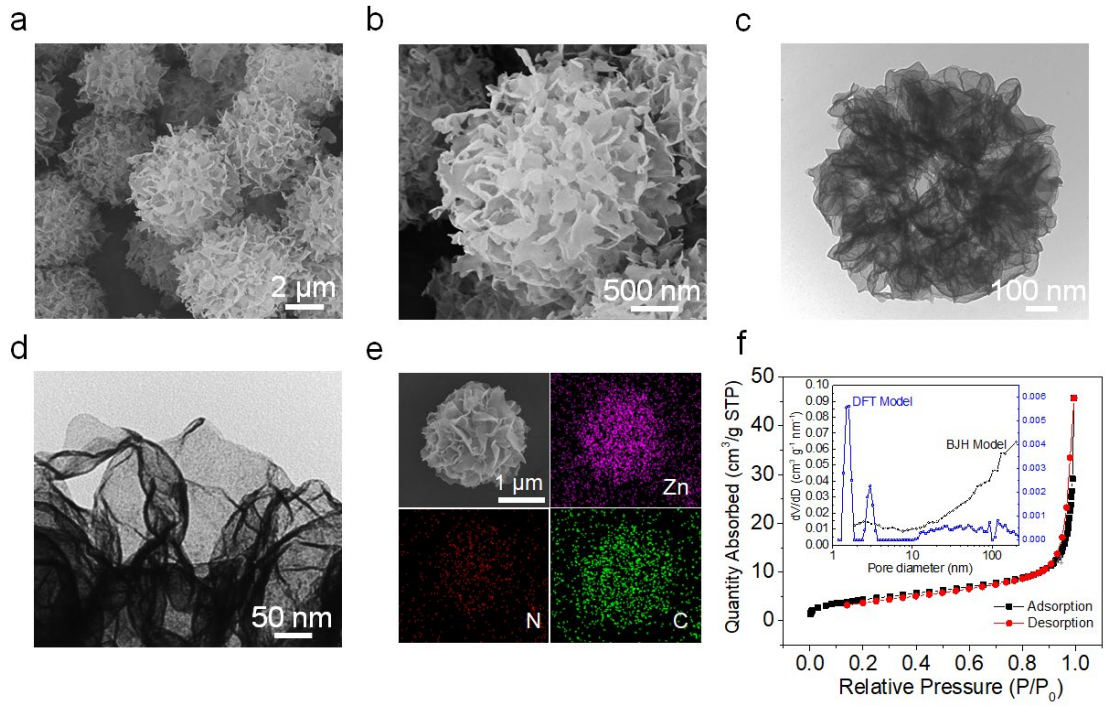

Figure 14 a) Low and b) high magnification SEM images of ZnHMT microflowers, c) TEM image of one ZnHMT microflower, d) TEM image of ZnHMT nanosheets, e) SEM image and the corresponding EDS mapping results of one ZnHMT microflower, f) N2 adsorption-desorption isothermal curves and the pore size distribution based on DFT calculation (blue line) and BJH calculation (black line)

Self-assembly process is well-known for their sensitivity to experimental conditions. Thereby, the impact of various experiment parameters (reactant molar ratio, temperature, time, and water content in solvent) were carefully investigated. It is found that ZnHMT microflowers can only be obtained when the molar ratio between $Zn(NO_3)_2$ and HMT is 2:1 (Figure 15b). When the molar ratio is too low (1:1), even ZnHMT nanosheets can't form (Figure 15a). Meanwhile, a too high molar ratio (4:1) bans the self-assembly progress (Figure 15c). It should be mentioned that the morphology of final products is very sensitive to water content. As little as 1 % water in ethanol solvent can completely ruin the self-assembly process (Figure 15e). When the water content was raised to 10%, the obtained ZnHMT nanosheets exhibit a rigid appearance with lateral size around 500 nm (Figure 15f). In addition, as it is depicted in Figure 16b, c, and d, the self-assembly of ZnHMT nanosheets can successfully proceed under a wide room temperature range (20-30℃). When the synthesis temperature is 0℃, very few microflowers with diameters around 6 μm can be found (Figure 16a). If the synthesis temperature is set to be 45℃, no microflowers but individual ZnHMT nanosheets can be attained (Figure 16e). The synthesis duration was found to have no influence on the formation of microflowers, indicating the self-assembly process is fast and thermal dynamically favored (Figure 17).

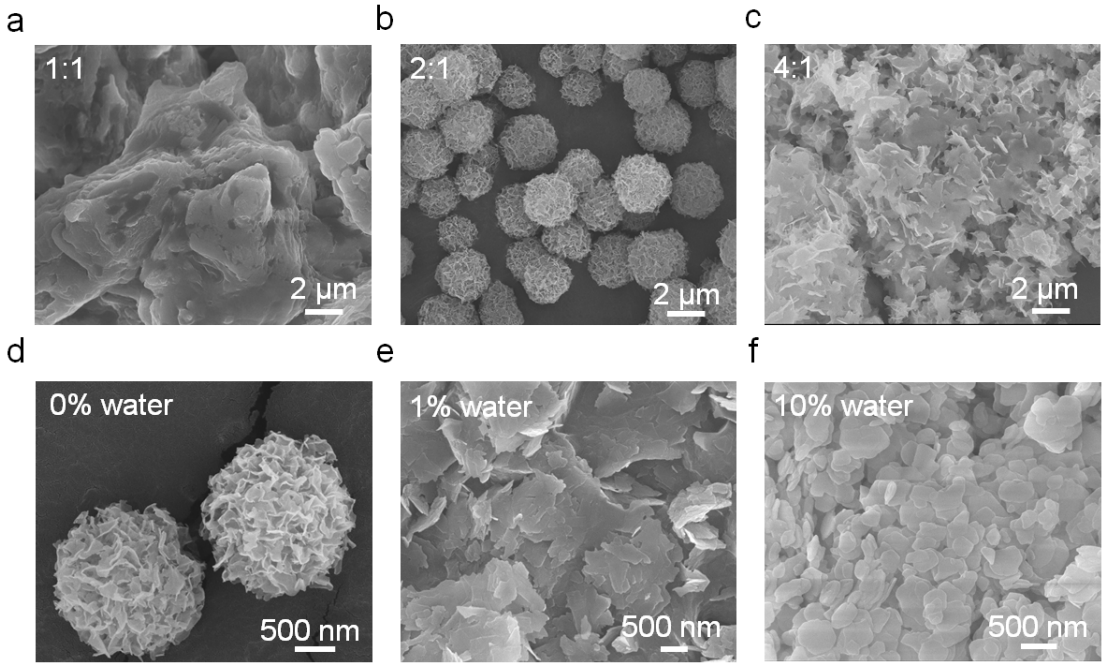

Figure 15 The morphology of ZnHMT with different reactant molar ratio between $Zn(NO_3)_2 \cdot 6H_2O$ and HMT: a) 1:1, b) 2:1, and c) 4:1. The morphology of ZnHMT with different water content: d) 0%, e) 1%, and f) 10%

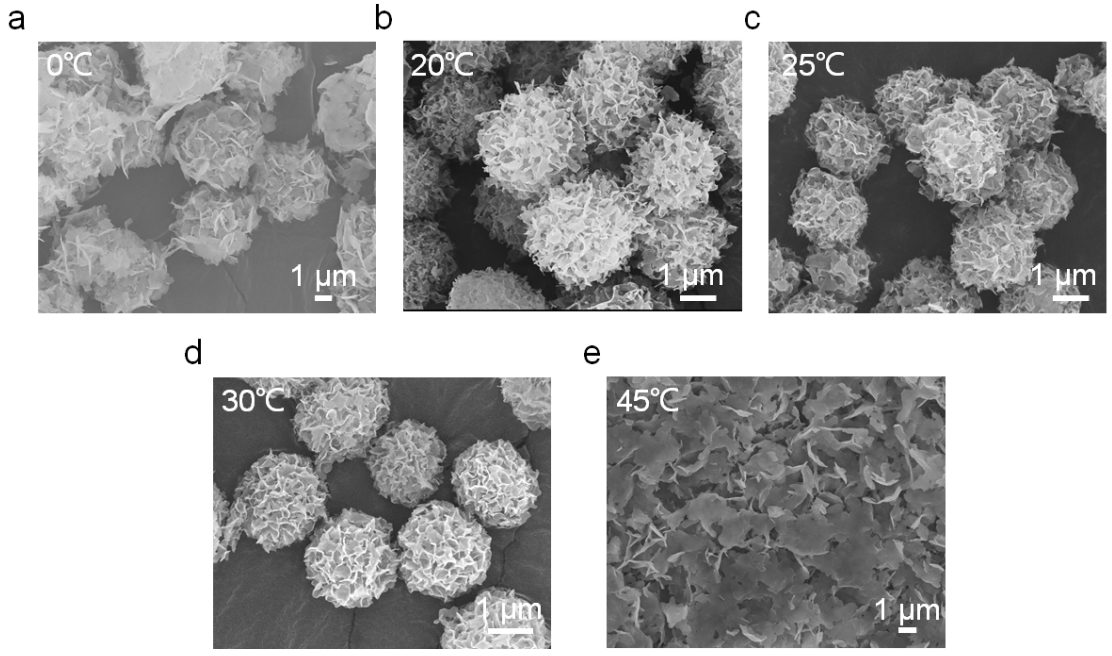

Figure 16 The morphology of ZnHMT synthesized under different temperature

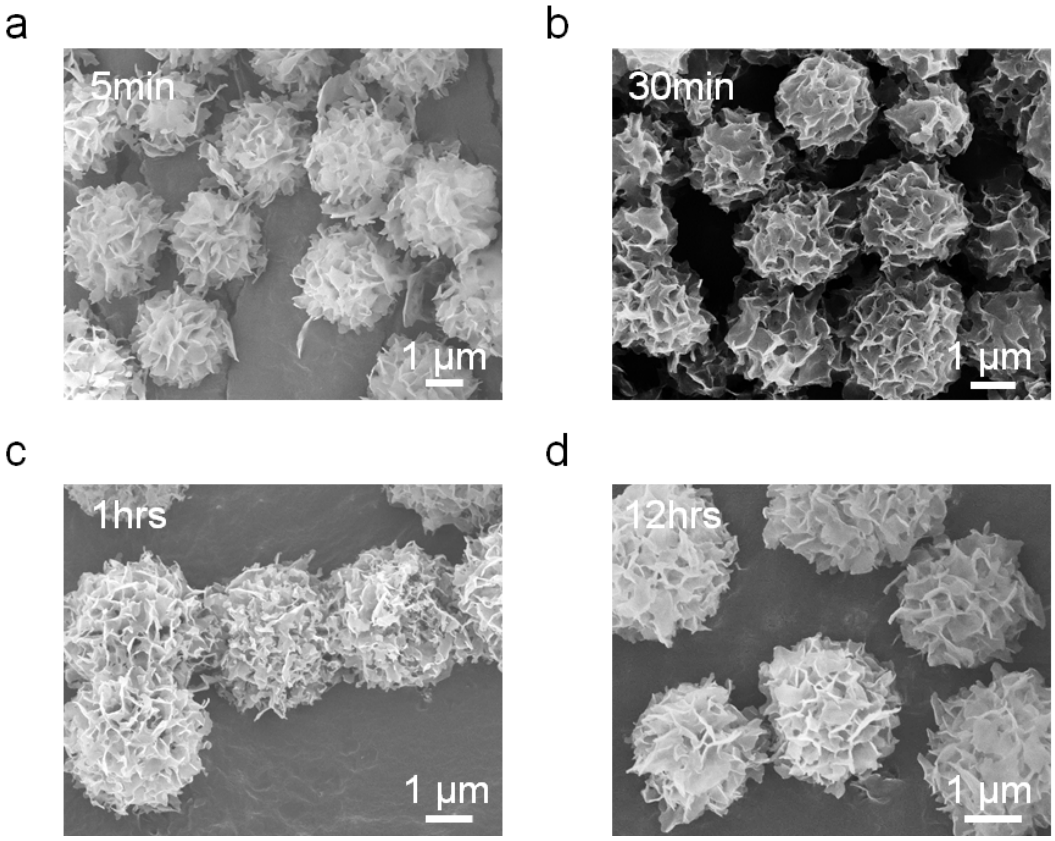

Figure 17 The morphology of ZnHMT synthesized with different reaction time

4. Improving the Performance of Li-S battery

4.1. Experimental Methods

4.1.1. Fabrication of Li_2S_6 Solution

3mL 0.5mol L^{-1} Li_2S_6 solution was synthesized by mixing 69mg Li_2S and 240mg S (the molar ratio is 1:5) with 3mL THF in a glass vial in a glove box. After sealing the glass vial with Teflon tape, the vial was first heated under 120℃ for 3 hours. Li_2S and S powder began to dissolve into the THF solvent, and the color of the solution changed into dark red. Then, to fully dissolve Li_2S and sulfur, the solution was heated at 60℃ overnight and 0.5 mol L^{-1} Li_2S_6 solution was obtained. The 0.5 mol L^{-1} Li_2S_6 solution was further diluted by THF to obtain 4.5mM and 20mM Li_2S_6 solution for polysulfide absorption test and polysulfide permeation test.

4.1.2. Polysulfide Absorption Test

20mg ZnHMT powder was added into 2ml 4.5mM Li_2S_6 solution in a glove box. After shaking, the mixture was stood still for 12 hours. The color change of the supernatant was recorded by a digital camera. To detect the remaining amount of Li_2S_6 in the solution, the supernatant was characterized by UV-vis spectroscopy. For comparison, identical procedure was performed for another same amount of Li_2S_6 solution without the addition

of ZnHMT.

In order to prove the existence of chemical interaction between ZnHMT microflower and Li_2S_6, XPS was conducted as well. The XPS samples were prepared as follow: 5mg ZnHMT powder was stirred in 2ml 4.5mM Li_2S_6 solution at 50℃ for 5 hours. The mixture was then poured into a glass plate and heated at 80℃ overnight to fully evaporate the THF solvent. The remaining dark purple powder was collected for the XPS test. For comparison, identical procedure was performed for another same amount of Li_2S_6 solution without the addition of ZnHMT. In the UV-vis and XPS spectra, the mixture of Li_2S_6 and ZnHMT was denoted as ZnHMT@Li_2S_6.

4.1.3. Fabrication of ZnHMT@PP Functional Separators

A black slurry containing 18mg ZnHMT powder, 18mg SP, and 4mg PVDF was synthesized using NMP as solvent. Then, the slurry was directly coated onto a PP membrane using the conventional doctor blade technique and subsequently dried in an oven at 60℃ for 12 hours. The functional separators, named as ZnHMT@PP separators, were obtained by pouching the ZnHMT-coated PP membrane. The areal mass loading and diameter of the ZnHMT@PP separators is 0.4-0.5mg/cm^2 and 18mm, respectively.

4.1.4. Polysulfide Permeation Test

A H-shaped glass cell was assembled using ZnHMT@PP or PP as separators. The same volume (about 25ml) of 20mM Li_2S_6 solution and THF solvent were added to the left and

right side of the glass cell, respectively. Digital photos were taken after various time to demonstrate the polysulfide blocking ability of the ZnHMT@PP separators.

4.1.5. Fabrication of Conventional Sulfur/Carbon Electrodes

First, S/SP composite was synthesized. 80mg SP and 160mg S powder were mixed and grinded thoroughly. The mixture was transferred into a glass vial, sealed under Ar atmosphere, and heated at 155℃ for 5 hours. Second, 40mg S/SP composite, 5mg SP, and 5mg PVDF were grinded together to form a slurry using NMP as solvent. The slurry was coated onto a carbon-coated aluminum foil and dried in an oven at 60℃ for 12 hours. Finally, the sulfur/carbon electrodes were obtained by pouching the as-prepared aluminum foil. The areal sulfur loading for the electrodes is around 1.2 mg/cm^2 and their diameter is 12 mm. The synthesis of high sulfur loading electrodes followed the same procedure, but the areal sulfur loading is around 4.5 mg/cm^2.

4.1.6. Electrochemical Characterization

In an argon-filled glove box, 2032 type coin cells were assembled to test the battery performance. The oxygen and water contents in the glove box were both below 0.5ppm. For battery assembly, a S/SP cathode was paired with pure lithium plate which acted as the anode. Regular PP separator or ZnHMT@PP separator was placed between the anode and cathode. The coating side of ZnHMT@PP separator was faced with the sulfur cathode. The cells with regular PP were named as PP cells, while the cells with ZnHMT@PP were referred to as ZnHMT@PP cells. The electrolyte was 1M bis(trifluoromethane)

sulfonimide lithium salt (LiTFSI) in the mixture of dimethoxymethane (DME) and 1,3-dioxolane (DOL) (1:1 in volume ratio) with the addition of 3wt% lithium nitrate. The total electrolyte volume for each coin cell is 25uL. Electrochemical Impedance spectroscopy was conducted on a Gamry 5000E workstation in the frequency of 0.1Hz to 10^6 Hz. CV was also performed on a Gamry 5000E workstation with the cutoff voltage at 1.8V and 2.6V. The scanning rate was set as 0.1mV s^{-1}.

Short term cycling was performed at 0.2C for 50 cycles to exhibit the polysulfide restriction ability of ZnHMT@PP separators. Long term cycling was conducted at 1C for 800 cycles to demonstrate the cycling stability of ZnHMT@PP cells. Rate performance was conducted under 0.2C, 0.5C, 1C, 2C, 5C, and back to 0.2C to study the current density impact on the reversibility of sulfur redox reactions. 10 cycles were performed at each rate. The voltage range for low current density is 1.8V to 2.6V. For high current density (>0.5C), the voltage range is 1.7V to 2.7V. For the post characterization, lithium foils and separators were extracted from the cells after 10 cycles, dried in a glove box overnight, and inspected by SEM. For the self-discharge test, PP cells and ZnHMT cells were first cycled for ten cycles. Then, they were stopped at full charged status, stood for 24 hours, and full discharged for one cycle.

4.2. Results and Discussions

4.2.1. The Interaction Between Polysulfide and ZnHMT Microflowers

Based on previous research reports we discussed in chapter 1, zinc and nitrogen elements in ZnHMT should possess strong Lewis acid-base interaction with polysulfides due to their polarity. To confirm this hypothesis, polysulfides absorption test was first conducted. After added ZnHMT into a Li_2S_6 solution, the color of the Li_2S_6 solution faded from dark red to light yellow after 12 hours, as is shown in the inset picture of Figure 18. This result visually proves that ZnHMT has a strong affinity with polysulfides. The supernatant of Li_2S_6 and Li_2S_6@ZnHMT solution was then characterized by an ultraviolet-visible spectrophotometer. In Figure 18, the absorption peak for THF solvent, which is at around 207nm, was found for both solutions. There are two board peaks at 341nm and 407nm for Li_2S_6 solution, corresponding to the S_6^{2-} and S_4^{2-} groups[73], respectively. In sharp contrast, both peaks disappeared for Li_2S_6@ZnHMT solution, indicating the absence of polysulfides in the solution and good consistent with the color variation in absorption test.

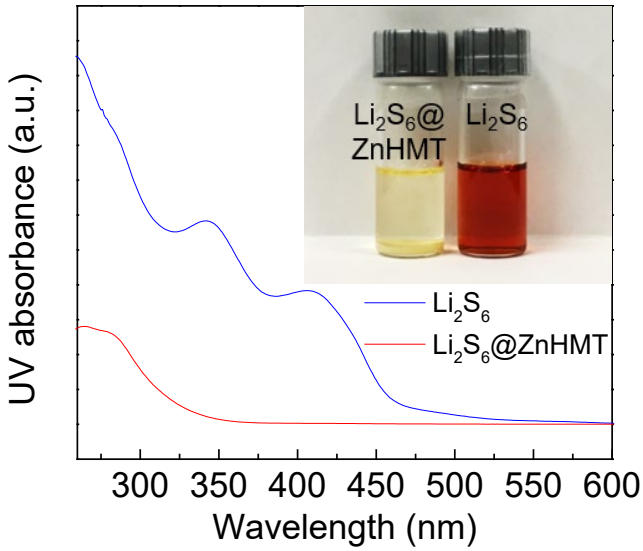

Figure 18 The UV-vis spectra for Li_2S_6 and Li_2S_6@ZnHMT; The inset picture is the corresponding optical photo

To further detect the affinity mechanism and chemical environment change between ZnHMT and polysulfides, XPS was conducted and the results for Li_2S_6 and ZnHMT@ Li_2S_6 were presented in Figure 19. In the S2p spectrum of Li_2S_6 (Figure 19a), the two pairs of peaks representing the terminal S_T^- and bridging S_B^- groups are observed, which are located at 161.3 eV and 162.9 eV respectively[74]. After the introduction of ZnHMT, both the above peaks shift to a higher binding energy. The strong Lewis acid-base interaction pushes sulfur's unpaired electrons into the free electron orbits provided by Zn and N atoms, which consequently increases the energy requirement to excite the remaining sulfur electrons during XPS test. Based on the same reason, peaks corresponding to the $NO3^-$, C-N bond, and Zn^{2+} in the N1S and Zn2p3/2 spectrum (Figure 19b and c) all move to lower binding energy accordingly. In addition, no new peaks can be found in the S2p spectrum of ZnHMT@Li_2S_6, inferring that ZnHMT is chemically stable with polysulfides. Regarding to the Li1s spectrum (Figure 19d), the peak representing the Li-S bond was found at 54.6eV for both samples[75]. The new peak located at 55.6eV for ZnHMT@Li_2S_6 sample corresponds to the formation of Li-N bond[76] contributed by the Li atoms from polysulfides and N atoms from HMT ligands.

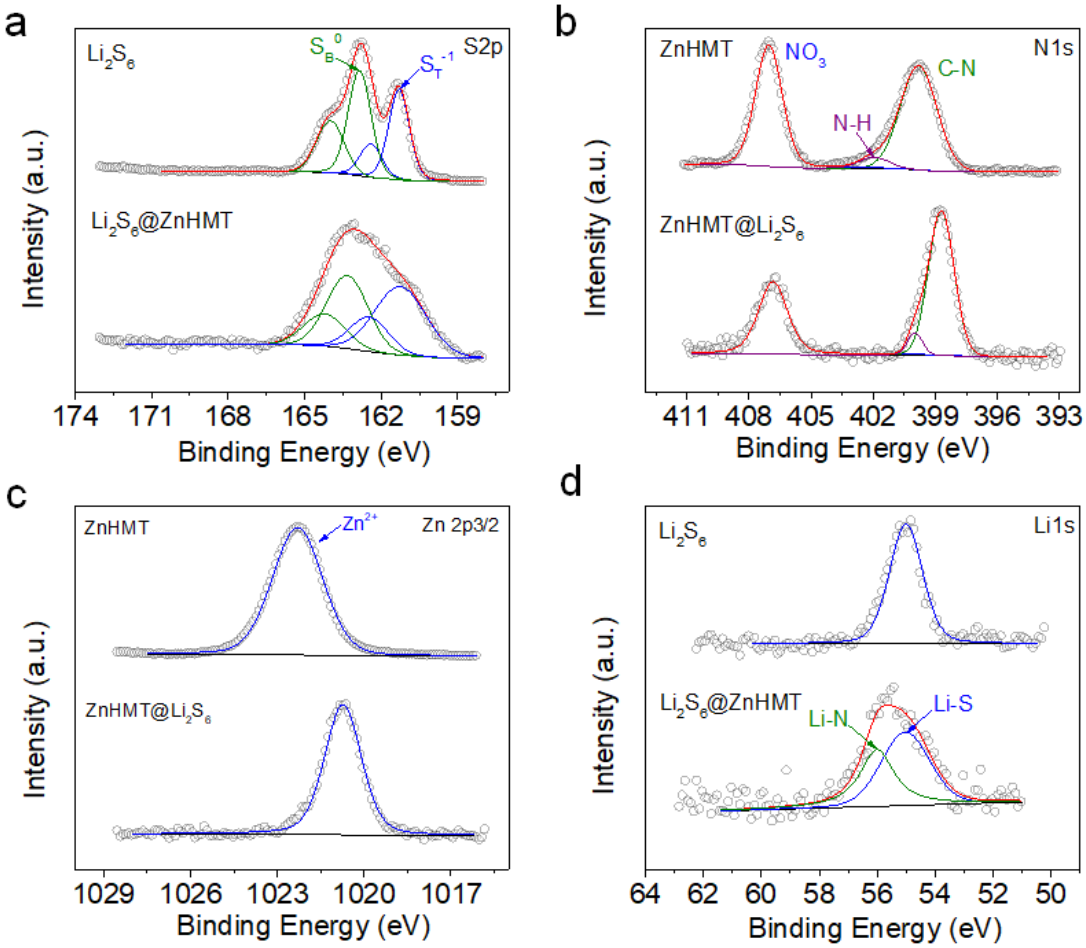

Figure 19 a) S2p, b) N1s, c) Zn2p3/2, d) Li1s XPS spectra for Li_2S_6 and ZnHMT@Li_2S_6

In short summary, based on the polysulfide absorption test and morphology characterization in Chapter 3, the strong polysulfide affinity of ZnHMT microflowers is achieved by two factors synergistically. First, as confirmed by the XPS results, there is a strong chemical interaction between ZnHMT and polysulfides. Both the metal nods and ligands in ZnHMT play an important role on refraining the movement of polysulfides. Additionally, it has been reported by other groups that ZnHMT possesses a high content of N and Zn (22.97wt% N and 17.88wt% Zn based on the formula of $[Zn(NO_3)_2(HMT)(H_2O)_2]_n$) [68], which ensures that each ZnHMT nanosheet own sufficient

absorption sites for polysulfides. Second, comparing to the traditional MOF bulks, the ultrathin 2D ZnHMT nanosheets can offer more polar sites and thereby increase the absorption efficiency. Moreover, the loosely assembled ZnHMT microflowers can avoid the common restacking problem for 2D MOF materials and offer enough space for long chain polysulfides[77]. Armed by the above advantages, ZnHMT microflowers should be a promising immobilizer for polysulfides in Li-S battery and able to greatly alleviate the notorious 'shuttling effect'.

4.2.2. Polysulfide Blocking Ability of ZnHMT@PP Separators

To embed ZnHMT microflowers into the system of Li-S batteries, a slurry composed of ZnHMT, SuperP (SP), and polyvinlidene fluoride (PVDF) was prepared and coated onto the conventional polypropylene (PP) separator using doctor blade technique. The modified separator is named as ZnHMT@PP separator. Figure 20a and 20b present the morphology of a PP separator and a ZnHMT@PP separator under the inspection of SEM. For PP separator, a great number of irregular pores can be observed with the diameter up to hundreds of nanometers. As the scheme in Figure 22b illustrates, polysulfides, with the diameter around 1.8nm[78], can readily migrate through these pores, causing severe side reactions and fast decay of battery performance. On contrary, the surface of ZnHMT@PP separator is free of pores. The inset picture of Figure 20b is the corresponding EDX mapping result for ZnHMT@PP separator. The uniform distribution of ZnHMT immobilizers will greatly suppress the probability that polysulfides migrate to the anode side. What's more, SP can also reutilize the polysulfides confined by ZnHMT, maintaining high sulfur utilization. Its high tortuosity can also functional as a physical barrier to

constrain polysulfides. To minimize the impact on battery's energy density, the thickness of ZnHMT@PP separators is controlled at around 2 um (Figure 20c) and the mass loading is 0.4-0.5mg/cm^2.

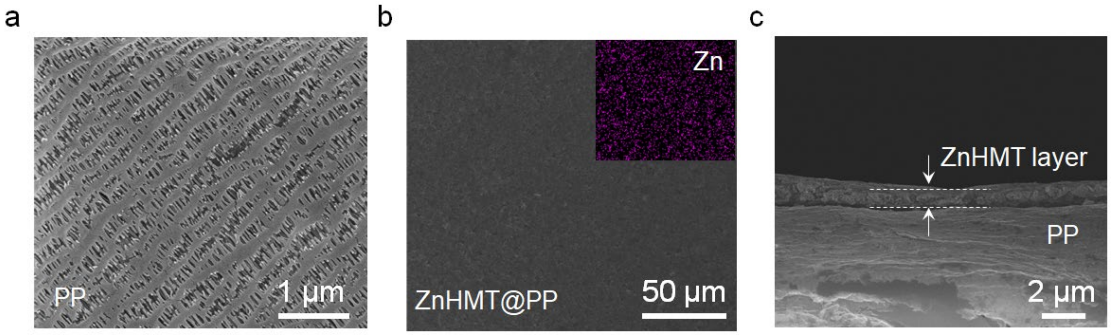

Figure 20 a) SEM image of the PP separator, b) SEM image and the corresponding EDX mapping result of the ZnHMT@PP separator, c) cross-section SEM image of ZnHMT@PP separator

Permeation experiment was conducted to manifest the polysulfide interception capability of the ZnHMT@PP separator. In order to simulate the actual environment in a Li-S battery, a H-shaped glass cell using a ZnHMT@PP separator or PP separator was assembled. As is displayed in Figure 21, same volume of Li_2S_6 THF solution (deep red color) and pure THF solvent (colorless) were added into the left and right side of the glass cell, respectively. In term of the cell using conventional PP separator, polysulfides began to reach the right side of the glass cell in less than 5 minutes. After merely 6 hours, the color of the right-side solution had changed from colorless to yellow completely, connoting the existence of a substantial amount of polysulfides and the lack of polysulfides blocking ability of the conventional PP separators (Figure 21b). In distinct comparison, by using the ZnHMT@PP separator, the right-side solution of the H-shaped cell remained as colorless even after 36

hours, exhibiting that polysulfides could not pass our functional coated separator. (Figure 21a)

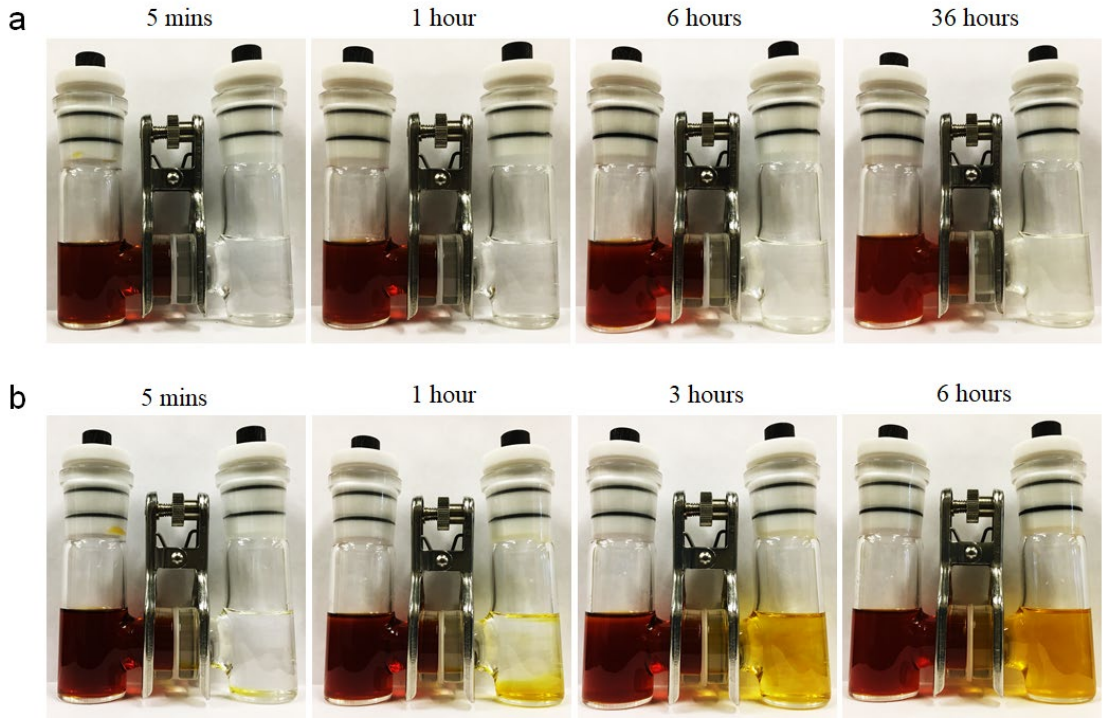

Figure 21 Polysulfide permeation experiment for a) ZnHMT@PP separator and b) PP separator, respectively

Figure 22a illustrates the Li-S battery configuration with the ZnHMT@PP separator. Supported by the absorption test and XPS characterization, ZnHMT microflowers equipped with substantial amount of absorption sites and pores can greatly retard the movement of polysulfides. Meanwhile, SP ensures the high reutilization of the absorbed polysulfides. The superior polysulfides blocking ability of the ZnHMT@PP separator was visually demonstrated by the permeation experiment. In conclusion, ZnHMT@PP separator is fully capable to impede polysulfides and thereby is expected to boost the electrochemical performance of Li-S battery comparing to the conventional PP separators.

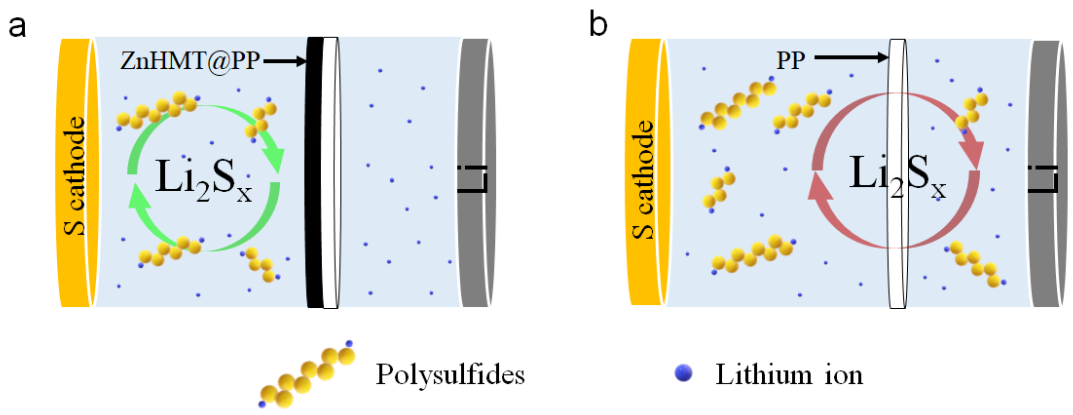

Figure 22 Scheme illustration for a) ZnHMT@PP cell and b) PP cell. The presence of ZnHMT@PP separator can greatly withhold the permeation of polysulfides from cathode area to anode area

4.2.3. Improving the Performance of Carbon-Based Cathodes

To evaluate their impact on the performance of Li-S batteries, batteries with ZnHMT@PP separators or regular PP separators were assembled using 2032 coin cells. Conventional sulfur cathodes were synthesized by the conventional doctor blade technique using a slurry containing S@SP composite, SP, and PVDF in the mass ratio of 8:1:1. Thermogravimetric analysis (Figure 23) prove that the sulfur content for S@SP composite is around 66.7 wt%. The areal sulfur loading for the cathodes is controlled to be around 1.2mg cm^{-2}.

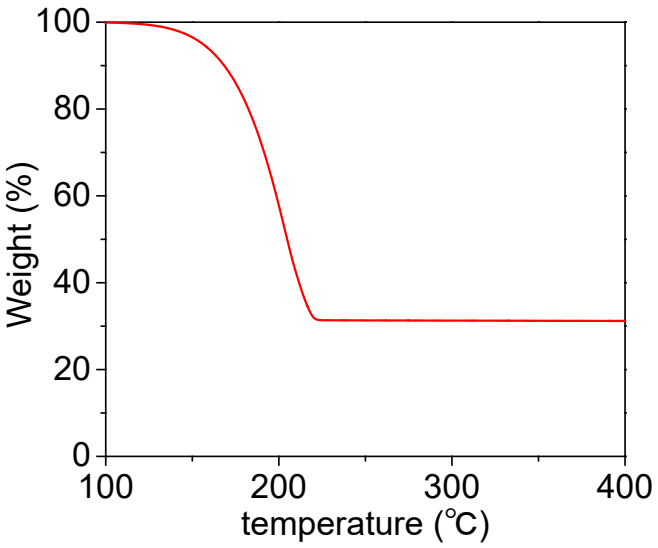

Figure 23 TGA result for S@SP composite

During the CV measurement, a Li-S battery with a carbon-based cathode shows two peaks in the cathodic scanning. The peak centered at around 2.3V is related to the reduction of elemental sulfur to the long chain polysulfides (Li_2S_x, x= 6~8). The further polysulfides conversion, from the soluble short chain polysulfides (Li_2S_x, x= 2~6) to the solid-state Li_2S_2 or Li_2S, can be assigned to the peak at around 2.0V. Equally, in the anodic scanning, a strong broad peak and an affiliated peak can be found at 2.3V and 2.4V, representing the reverse reduction reactions. The positions and area size of peaks directly indicate the kinetic condition of the polysulfides conversion reactions. Figure 24a is the cyclic voltammetry results for cells equipped with PP separators and ZnHMT@PP separators. The measurement was performed within the potential range of 1.8-2.6V at a scan rate of 0.1mV s^{-1}. Both cells exhibit the conventional curves which are identical to what we have just discussed above. For the PP cell, the positions of the cathodic peaks are at 2.00V and 2.27V. On the other hand, the positions of the corresponding peaks for the ZnHMT@PP

cell, shifting to lower voltage, are at 2.04V and 2.31V. Moreover, the ZnHMT@PP cell possesses narrower cathodic peaks and larger area size than that of the PP cell. Therefore, the ZnHMT@PP cell is more sensitive to voltage variation and can deliver higher capacity comparing to that of the PP cell under same condition. This conclusion can be made based on the anodic scanning result as well. Comparing to the PP separator, ZnHMT@PP separators can confine polysulfides in the cathode region, suppress the increase of inner resistance, and enhance the utilization of sulfur, all of which endow ZnHMT@PP cells with much better kinetic condition and performance.

The impact of the ZnHMT@PP separators on the conductivity of Li-S cells was explored by electrochemical impedance spectroscopy (EIS). In Figure 24b, fresh cells with the ZnHMT@PP separator or PP separator exhibit similar curves in the Nyquist plot. At high frequency, the intersection of the curve and the X axis is the contact resistance between the electrode and electrolyte (R_o). The diameter of the semicircle at high to mediate frequency represents the resistance of charge transfer (R_{ct})[79]. As both cells using the same type of 2032 coin cells, the value of R_o is similar. Nonetheless, for the cell with the ZnHMT@PP separator, the diameter of the semicircle is much smaller comparing to that of the PP cell. This reveals a faster transport rate of electrons and lithium ions in the electrodes, which agrees well with the CV results. The entrapment of polysulfides thanks to the ZnHMT microflowers reduces the resistance of battery while the porous hierarchical microflower structure enables the fast transportation of lithium ions.

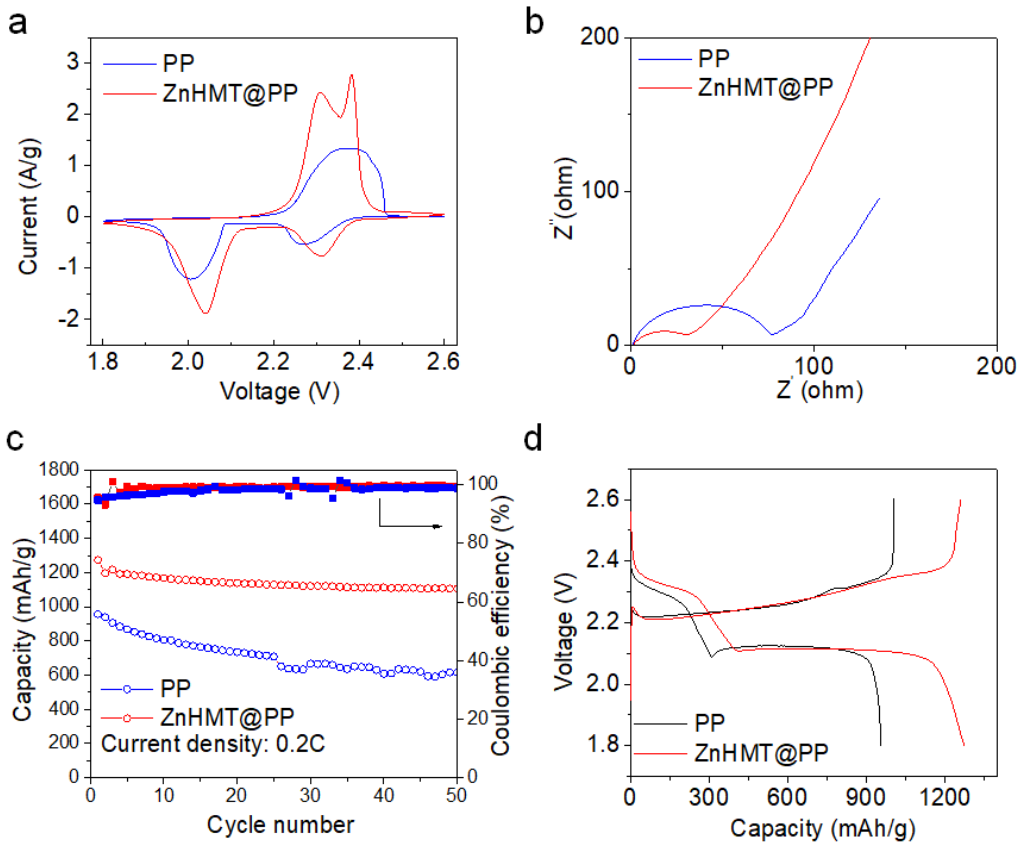

Figure 24 a) CV curve, b) EIS spectrum for fresh cells, c) short term cycling, d) the first cycle galvanostatic discharge-charge curve of ZnHMT@PP cell under 0.2C

Figure 24c and 24d are the short-term cycling profile and the corresponding galvanostatic discharge-charge profile at first cycle. The two distinct discharge plateaus with different capacity and the two overlapped charge plateaus are in consistency with the CV results in Figure 24a. At the current density of 0.2C, the capacity of the ZnHMT@PP cell starts from 1273.8 mAh g^{-1} and slowly decreases to 1106.9 mAh g^{-1} after 50 cycles. The capacity decay rate is 0.26% per cycle. On the other hand, the capacity of the PP cell fails sharply from 1013.2 mAh g^{-1} to 694.1 mAh g^{-1}, with nearly three times faster capacity decay rate per cycle. The slow capacity decay for the ZnHMT@PP cell suggests the excellent

confinement of polysulfides in the cathode region during battery cycling, which is in accordance with the polysulfides permeation experiment in Figure 21.

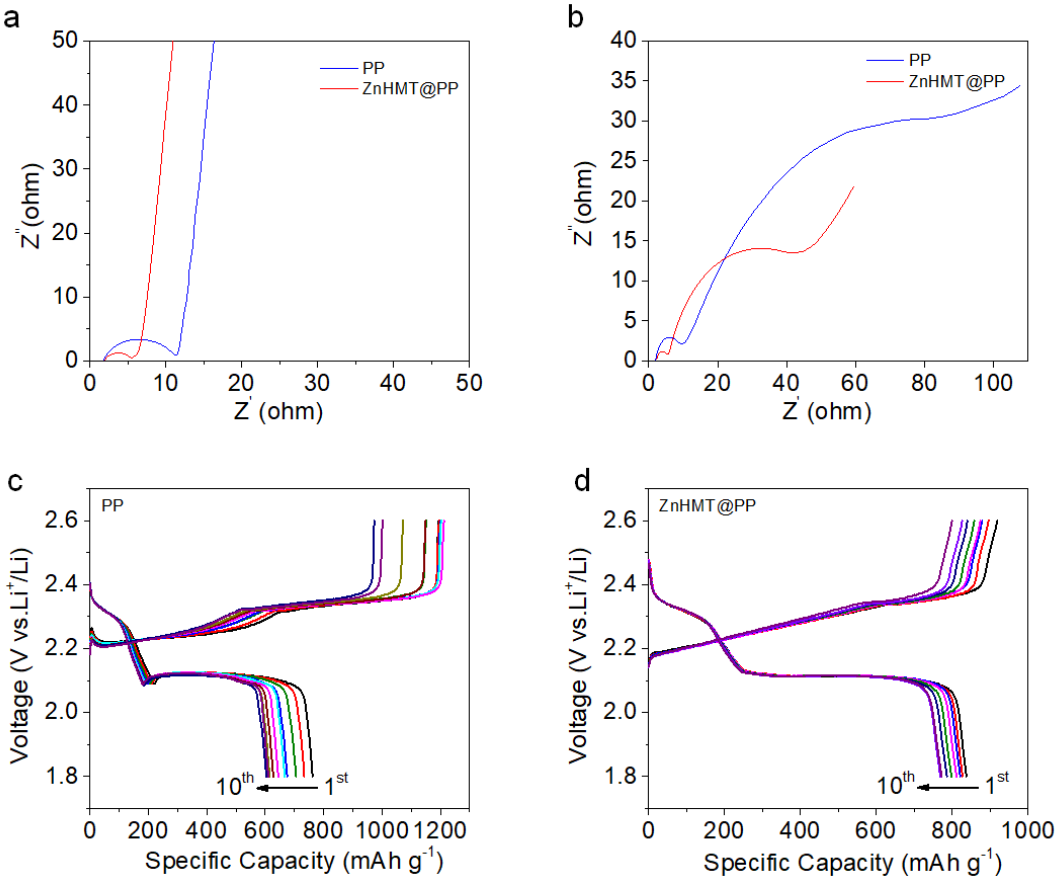

Figure 25 Nyquist plot for ZnHMT@PP cell and PP cell at a) full charge status and b) full discharge status. Discharge-charge galvanostatic curves for c) PP cells and d) ZnHMT@PP cells without the addition of lithium nitrate in the electrolyte

In Figure 25a and b, EIS spectra exhibits that the ZnHMT@PP cells also own lower charge transfer resistance under either fully charge or discharge status. The larger R_{ct} for the PP cells indicates the accumulation of the insulated byproduct on the surface of lithium anodes, owing to the corrosion of polysulfides. Lithium nitrate, a well-known additive for Li-S battery electrolyte, can protect the lithium anodes against the side reactions with

polysulfides and substantially enhance the Coulombic efficiency of Li-S battery[80-81]. In order to exclude this benign impact, cells with different separators were also assembled without the addition of lithium nitrate. As is displayed in Figure 25c and d, the Coulombic efficiency of the ZnHMT@PP cell is considerably higher than that of the PP Cell, indicating that there is less corrosion happening on the lithium anode. In other words, ZnHMT@PP separator plays an important role in inhibiting the permeation of polysulfides and enhancing sulfur utilization.

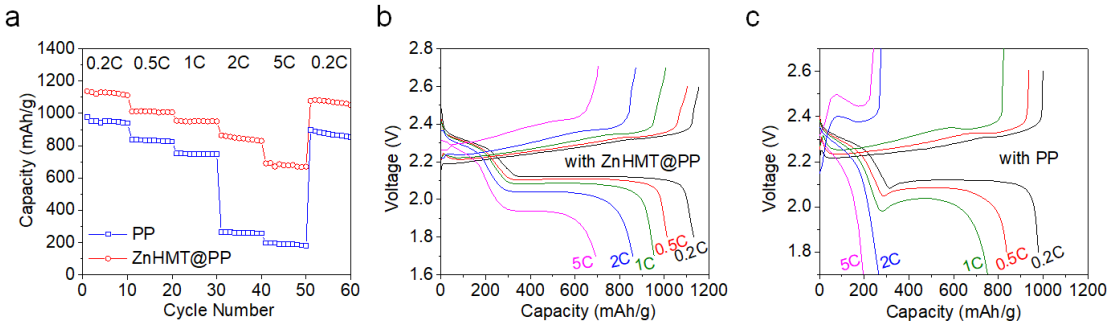

Figure 26 a) Rate performance comparison for ZnHMT@PP cell and PP cell. The corresponding galvanostatic discharge-charge curve of b) ZnHMT@PP cell and c) PP cell under different current density

Under high current density, the negative effect caused by the insulated sulfur and polysulfides shuttling will be amplified greatly, resulting in high polarization and low battery capacity. Therefore, multi-rate measurement was performed for the ZnHMT@PP cells and PP cells. As it is displayed in Figure 26a, under the current density of 0.2C, 0.5C, 1C, 2C, and 5C, the discharge capacity of the ZnHMT@PP cell is 1137.44, 1012.63, 954.63, 864.36, and 690.49 mAh g^{-1}, respectively. In the corresponding galvanostatic discharge curve (Figure 26b and c), the ZnHMT@PP cell can still show the standard two discharge

plateaus even at 2C and 5C. When switching the current density back to 0.2C, the ZnHMT@PP cell can still deliver a high reversible capacity of 1077.77 mAh g^{-1}. The unique hierarchical microflower structure entails short diffusion pathway for lithium ions while tremendous absorption sites on each ultrathin nanosheet successfully retard the movement of polysulfides, synergistically endowing ZnHMT@PP cells with outstanding performance at various current density. Unfortunately, owning to the increasing internal resistance caused by polysulfides, the discharge capacity of the PP cell is more than 3 times less than that of the ZnHMT@PP cell at 2C and 5C, implying high polarization and low utilization of the active material.

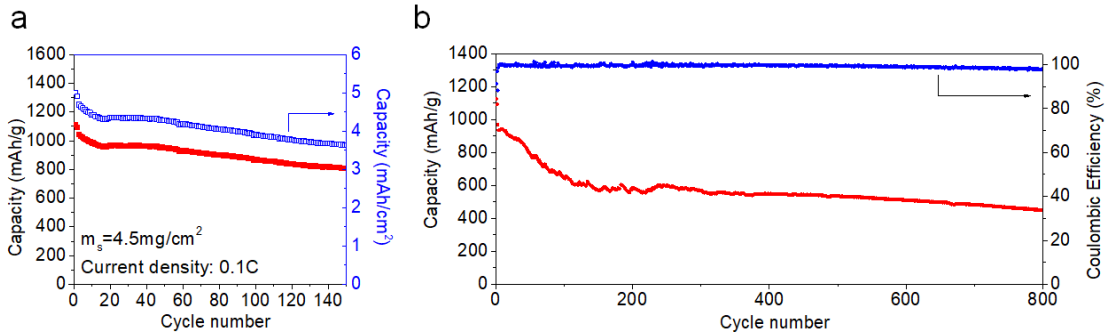

Figure 27 a) Cycling performance of the ZnHMT@PP cell with a high loading cathode, and b) long term cycling stability of the ZnHMT@PP cell at 1C

In Figure 27a, the long-term cycling stabilities of the ZnHMT@PP cells was evaluated at the current density of 1C. After few cycles of activation, the ZnHMT@PP cell can deliver an initial capacity of 969.1 mAh g^{-1}. The cell can still deliver a capacity of 448.6 mAh g^{-1} after 800 cycles with the capacity fading at 0.07% per cycle and the average Coulombic efficiency is above 99%. Hence, our ZnHMT@PP separators can effectively retard the shuttling of polysulfides, stimulate the complete conversion of sulfur, and increase the

lifespan of the Li-S battery. In order to manifest the potential of ZnHMT@PP separator in practical application, electrochemical measurement for Li-S batteries with high sulfur loading cathodes were also performed (Figure 27b). The areal sulfur loading is controlled at 4.5mg cm^{-2} and the cells were tested under 0.1C. The initial discharge capacity for the high loading ZnHMT@PP cells was 1125.22 mAh g^{-1} (5.00 mAh cm^{-2}), implying the high utilization of the active material. After 150 cycles, the discharge capacity is 817.64 mAh g^{-1} (3.64 mAh cm^{-2}) with a capacity retention of 73%.

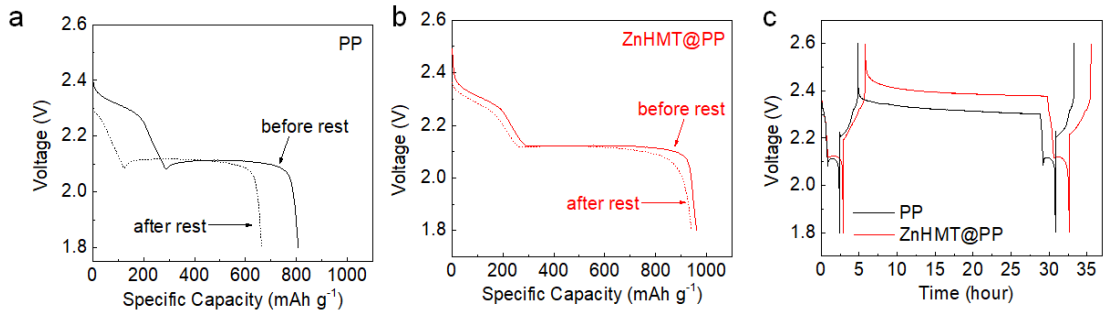

Figure 28 The discharge curves before and after 24 hours rest for a) PP cells and b) ZnHMT@PP cells, c) overall voltage-time profiles comparison during the self-discharge test

During the open circuit status, sulfur or polysulfides in the cathode tend to dissolve into electrolyte, migrate to the anode side due to the concentration gradient, and directly react with the lithium anode, which greatly reduces the battery capacity and open circuit voltage. This phenomenon is known as the self-discharge behavior of Li-S batteries[82]. The introduction of the ZnHMT@PP separator should be able to immobilize the polysulfides among the cathode area and subsequently alleviate this notorious phenomenon. Self-discharge experiment was conducted to test this hypothesis. After ten cycles at 0.2C, both the PP cell and the ZnHMT@PP cell were stopped at full charge status and rested for 24

hours to study their self-discharge behavior. As is presented in Figure 28a and b, after rest, the PP cell suffered a huge capacity loss (144mAh g^{-1}) in the subsequent discharge stage while the capacity of the ZnHMT@PP cell merely lost 19.9 mAh g^{-1}. Accordingly, in Figure 28c, the open circuit voltage for the PP cell is also substantially lower than that of the ZnHMT@PP cell. Above results confirm our hypothesis that ZnHMT@PP separators can greatly moderate the self-discharge behavior as it is capable to hinder the shuttling of polysulfides.

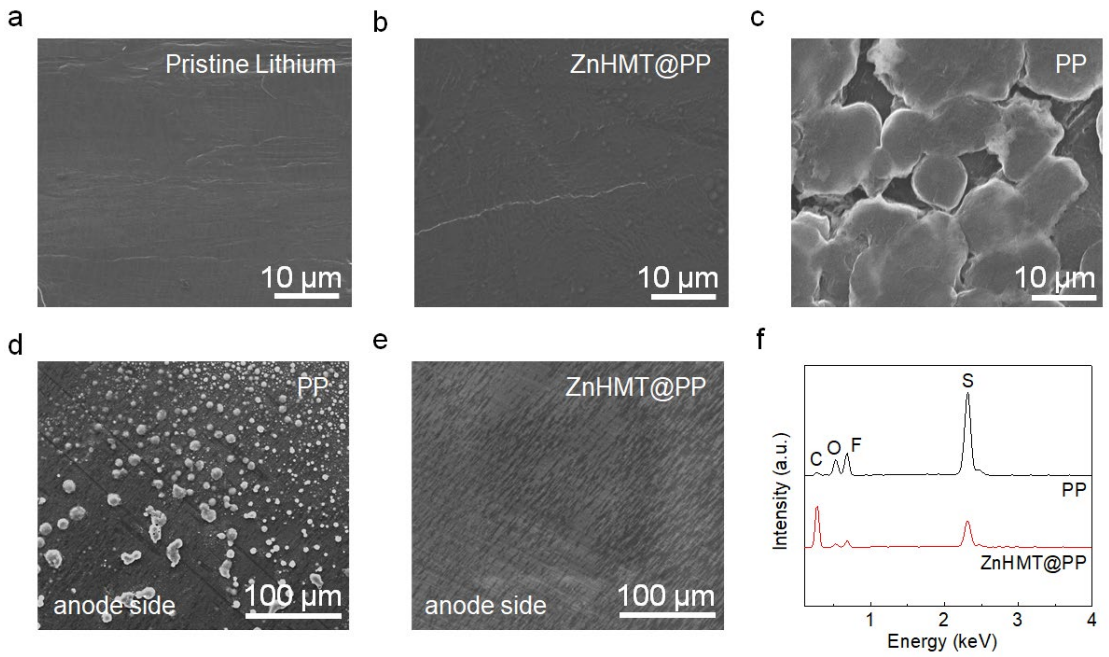

Figure 29 SEM images of a) pristine lithium plate, lithium plates extracted from b) the ZnHMT@PP cell and c) the PP cell. The anode side SEM images of d) the PP separator and e) the ZnHMT@PP separator after cycling, f) EDX spectra of the two separators

What's more, the lithium anodes and the separators for the PP cells and the ZnHMT@PP cells were extracted after cycling and examined by SEM. In Figure 29c, plenty of swells are found on the surface of the lithium plate from the PP cell, which is the byproducts

caused by the corrosion of polysulfides. This insulated byproduct will keep accumulating on the anode surface during the battery cycling and constantly increase cell's inner resistance and decrease the Coulombic efficiency, which is in good consistent with Figure 25c. Even worse, these swells can provoke the formation of sharp lithium dendrites, which can pierce through the separator and cause severe battery explosion[83]. Comparatively, the lithium plate from the ZnHMT@PP cell shows a much smoother morphology (Figure 25b), which is similar to the surface of pristine lithium plate (Figure 25a). This result implies the absence of polysulfides in the anode region and an effective protection for the lithium anode, contributed by the presence of ZnHMT@PP separators. A more explicit evidence is the anode side morphology of the two separators. In Figure 25d, a great number of small particles had formed on the PP separator as its pores could not withhold the shuttling of polysulfides. Nevertheless, in Figure 25e, the surface of the ZnHMT@PP separator was quite clean without any precipitations. These results agree well with the surface morphology of the lithium anodes in Figure 25b and c. To quantitively compare the content of sulfur on the above separators, EDX spectra was also performed. As is presented in Figure 25f, without any surprise, the PP separator had a much higher sulfur content. All in all, both the self-discharge test and post characterization verified again that ZnHMT@PP separators own high capability to restrain polysulfides, which is in consistent with the results from the permeation experiments and battery performance.

5. Conclusions

In conclusion, a novel hierarchical ZnHMT microflower structure, constructed through the self-assembly of ultrathin random oriented 2D nanosheets, is fabricated by a facile procedure. The XPS and absorption test confirmed the existence of a strong Lewis acid base interaction between ZnHMT and polysulfides. Besides, the 3D hierarchical microflower structure helps to maximize the number of absorption sites for polysulfides and accelerate ion diffusion rate. When ZnHMT microflowers were decorated as immobilizers onto the conventional PP separators, the notorious polysulfides shuttling effect and the self-discharge behavior for Li-S batteries were greatly suppressed. As a consequence, when using the simple S/C cathodes, the Li-S batteries with the ZnHMT@PP separators achieved an excellent rate capability and cycling stability, ie, a capacity of 690.49mAh g^{-1} at 5C, a capacity decay rate of 0.07 % per cycle after 800 cycles at 1C, and a high areal capacity of 5mAh cm^{-2}. This work provides not only a novel morphology for the MOF family, but also a new candidate for the functional separators strategy in order to boost the performance of Li-S batteries.

6. References

1. Statistical Review of World Energy. https://www.bp.com/en/global/corporate/energy-economics/statistical-review-of-world-energy.html.

2. Tarascon, J. M.; Armand, M., Issues and challenges facing rechargeable lithium batteries. *Nature* **2001,** *414* (6861), 359-367.

3. Mehta, V.; Cooper, J. S., Review and analysis of PEM fuel cell design and manufacturing. *Journal of Power Sources* **2003,** *114* (1), 32-53.

4. Wang, G.; Zhang, L.; Zhang, J., A review of electrode materials for electrochemical supercapacitors. *Chem Soc Rev* **2012,** *41* (2), 797-828.

5. Manthiram, A.; Fu, Y.; Chung, S. H.; Zu, C.; Su, Y. S., Rechargeable lithium-sulfur batteries. *Chem Rev* **2014,** *114* (23), 11751-87.

6. Lee, J.-S.; Tai Kim, S.; Cao, R.; Choi, N.-S.; Liu, M.; Lee, K. T.; Cho, J., Metal-Air Batteries with High Energy Density: Li-Air versus Zn-Air. *Advanced Energy Materials* **2011,** *1* (1), 34-50.

7. Aurbach, D.; Zinigrad, E.; Cohen, Y.; Teller, H., A short review of failure mechanisms of lithium metal and lithiated graphite anodes in liquid electrolyte solutions. *Solid State Ionics* **2002,** *148* (3-4), 405-416.

8. Armand, M. B., Intercalation Electrodes. In *Materials for Advanced Batteries*, Murphy, D. W.; Broadhead, J.; Steele, B. C. H., Eds. Springer US: Boston, MA, 1980; pp 145-161.

9. Hausbrand, R.; Cherkashinin, G.; Ehrenberg, H.; Gröting, M.; Albe, K.; Hess, C.; Jaegermann, W., Fundamental degradation mechanisms of layered oxide Li-ion battery cathode materials: Methodology, insights and novel approaches. *Materials Science and Engineering: B* **2015,** *192*, 3-25.

10. Zhang, Y. C.; Wang, C. Y., Cycle-Life Characterization of Automotive Lithium-Ion Batteries with LiNiO2 Cathode. *Journal of the Electrochemical Society* **2009,** *156* (7), A527-A535.

11. Ammundsen, B.; Desilvestro, J.; Groutso, T.; Hassell, D.; Metson, J. B.; Regan, E.; Steiner, R.; Pickering, P. J., Formation and structural properties of layered LiMnO2 cathode

materials. *Journal of the Electrochemical Society* **2000,** *147* (11), 4078-4082.

12. Nitta, N.; Wu, F.; Lee, J. T.; Yushin, G., Li-ion battery materials: present and future. *Materials Today* **2015,** *18* (5), 252-264.

13. Idota, Y.; Kubota, T.; Matsufuji, A.; Maekawa, Y.; Miyasaka, T., Tin-based amorphous oxide: A high-capacity lithium-ion-storage material. *Science* **1997,** *276* (5317), 1395-1397.

14. Chan, C. K.; Peng, H. L.; Liu, G.; McIlwrath, K.; Zhang, X. F.; Huggins, R. A.; Cui, Y., High-performance lithium battery anodes using silicon nanowires. *Nature Nanotechnology* **2008,** *3* (1), 31-35.

15. Chung, S.-H.; Chang, C.-H.; Manthiram, A., Progress on the Critical Parameters for Lithium-Sulfur Batteries to be Practically Viable. *Advanced Functional Materials* **2018,** *28* (28).

16. Aurbach, D.; Zaban, A.; Gofer, Y.; Ely, Y. E.; Weissman, I.; Chusid, O.; Abramson, O., Recent studies of the lithium-liquid electrolyte interface Electrochemical, morphological and spectral studies of a few important systems. *Journal of Power Sources* **1995,** *54* (1), 76-84.

17. Gao, J.; Lowe, M. A.; Kiya, Y.; Abruna, H. D., Effects of Liquid Electrolytes on the Charge-Discharge Performance of Rechargeable Lithium/Sulfur Batteries: Electrochemical and in-Situ X-ray Absorption Spectroscopic Studies. *J. Phys. Chem. C* **2011,** *115* (50), 25132-25137.

18. Chung, S. H.; Manthiram, A., Current Status and Future Prospects of Metal-Sulfur Batteries. *Adv Mater* **2019**, e1901125.

19. Ji, X.; Lee, K. T.; Nazar, L. F., A highly ordered nanostructured carbon-sulphur cathode for lithium-sulphur batteries. *Nat Mater* **2009,** *8* (6), 500-6.

20. Ji, X. L.; Nazar, L. F., Advances in Li-S batteries. *J Mater Chem* **2010,** *20* (44), 9821-9826.

21. Fan, L.; Li, M.; Li, X.; Xiao, W.; Chen, Z.; Lu, J., Interlayer Material Selection for Lithium-Sulfur Batteries. *Joule* **2019,** *3* (2), 361-386.

22. Xin, S.; Gu, L.; Zhao, N.-H.; Yin, Y.-X.; Zhou, L.-J.; Guo, Y.-G.; Wan, L.-J., Smaller Sulfur Molecules Promise Better Lithium–Sulfur Batteries. *Journal of the American Chemical Society* **2012,** *134* (45), 18510-18513.

23. Moon, S.; Jung, Y. H.; Jung, W. K.; Jung, D. S.; Choi, J. W.; Kim, D. K., Encapsulated

Monoclinic Sulfur for Stable Cycling of Li–S Rechargeable Batteries. *Advanced Materials* **2013,** *25* (45), 6547-6553.

24. Yin, Y.-X.; Xin, S.; Guo, Y.-G.; Wan, L.-J., Lithium–Sulfur Batteries: Electrochemistry, Materials, and Prospects. *Angewandte Chemie International Edition* **2013,** *52* (50), 13186-13200.

25. Zhang, B.; Qin, X.; Li, G. R.; Gao, X. P., Enhancement of long stability of sulfur cathode by encapsulating sulfur into micropores of carbon spheres. *Energy & Environmental Science* **2010,** *3* (10).

26. Schuster, J.; He, G.; Mandlmeier, B.; Yim, T.; Lee, K. T.; Bein, T.; Nazar, L. F., Spherical ordered mesoporous carbon nanoparticles with high porosity for lithium-sulfur batteries. *Angew Chem Int Ed Engl* **2012,** *51* (15), 3591-5.

27. Huang, X.; Tang, J.; Luo, B.; Knibbe, R.; Lin, T.; Hu, H.; Rana, M.; Hu, Y.; Zhu, X.; Gu, Q.; Wang, D.; Wang, L., Sandwich-Like Ultrathin TiS2 Nanosheets Confined within N, S Codoped Porous Carbon as an Effective Polysulfide Promoter in Lithium-Sulfur Batteries. *Advanced Energy Materials* **2019**.

28. Zhang, C.; Wu, H. B.; Yuan, C.; Guo, Z.; Lou, X. W., Confining sulfur in double-shelled hollow carbon spheres for lithium-sulfur batteries. *Angew Chem Int Ed Engl* **2012,** *51* (38), 9592-5.

29. Yuan, L.; Yuan, H.; Qiu, X.; Chen, L.; Zhu, W., Improvement of cycle property of sulfur-coated multi-walled carbon nanotubes composite cathode for lithium/sulfur batteries. *Journal of Power Sources* **2009,** *189* (2), 1141-1146.

30. Guo, J. C.; Xu, Y. H.; Wang, C. S., Sulfur-Impregnated Disordered Carbon Nanotubes Cathode for Lithium-Sulfur Batteries. *Nano Lett.* **2011,** *11* (10), 4288-4294.

31. Cao, Y.; Li, X.; Aksay, I. A.; Lemmon, J.; Nie, Z.; Yang, Z.; Liu, J., Sandwich-type functionalized graphene sheet-sulfur nanocomposite for rechargeable lithium batteries. *Phys Chem Chem Phys* **2011,** *13* (17), 7660-5.

32. Wang, H. L.; Yang, Y.; Liang, Y. Y.; Robinson, J. T.; Li, Y. G.; Jackson, A.; Cui, Y.; Dai, H. J., Graphene-Wrapped Sulfur Particles as a Rechargeable Lithium-Sulfur Battery Cathode Material with High Capacity and Cycling Stability. *Nano Lett.* **2011,** *11* (7), 2644-2647.

33. Chung, S.-H.; Manthiram, A., Bifunctional Separator with a Light-Weight Carbon-

Coating for Dynamically and Statically Stable Lithium-Sulfur Batteries. *Advanced Functional Materials* **2014,** *24* (33), 5299-5306.

34. Chang, C. H.; Chung, S. H.; Manthiram, A., Effective Stabilization of a High-Loading Sulfur Cathode and a Lithium-Metal Anode in Li-S Batteries Utilizing SWCNT-Modulated Separators. *Small* **2016,** *12* (2), 174-9.

35. Shaibani, M.; Akbari, A.; Sheath, P.; Easton, C. D.; Banerjee, P. C.; Konstas, K.; Fakhfouri, A.; Barghamadi, M.; Musameh, M. M.; Best, A. S.; Ruther, T.; Mahon, P. J.; Hill, M. R.; Hollenkamp, A. F.; Majumder, M., Suppressed Polysulfide Crossover in Li-S Batteries through a High-Flux Graphene Oxide Membrane Supported on a Sulfur Cathode. *ACS Nano* **2016,** *10* (8), 7768-79.

36. Zhou, X.; Liao, Q.; Bai, T.; Yang, J., Nitrogen-doped microporous carbon from polyaspartic acid bonding separator for high performance lithium-sulfur batteries. *Journal of Electroanalytical Chemistry* **2017,** *791*, 167-174.

37. Zhou, X.; Liao, Q.; Bai, T.; Yang, J., Rational design of graphene @ nitrogen and phosphorous dual-doped porous carbon sandwich-type layer for advanced lithium–sulfur batteries. *Journal of Materials Science* **2017,** *52* (13), 7719-7732.

38. Paraknowitsch, J. P.; Thomas, A., Doping carbons beyond nitrogen: an overview of advanced heteroatom doped carbons with boron, sulphur and phosphorus for energy applications. *Energy & Environmental Science* **2013,** *6* (10), 2839-2855.

39. Ji, L.; Rao, M.; Zheng, H.; Zhang, L.; Li, Y.; Duan, W.; Guo, J.; Cairns, E. J.; Zhang, Y., Graphene Oxide as a Sulfur Immobilizer in High Performance Lithium/Sulfur Cells. *Journal of the American Chemical Society* **2011,** *133* (46), 18522-18525.

40. Hou, T. Z.; Chen, X.; Peng, H. J.; Huang, J. Q.; Li, B. Q.; Zhang, Q.; Li, B., Design Principles for Heteroatom-Doped Nanocarbon to Achieve Strong Anchoring of Polysulfides for Lithium-Sulfur Batteries. *Small* **2016,** *12* (24), 3283-91.

41. Balach, J.; Singh, H. K.; Gomoll, S.; Jaumann, T.; Klose, M.; Oswald, S.; Richter, M.; Eckert, J.; Giebeler, L., Synergistically Enhanced Polysulfide Chemisorption Using a Flexible Hybrid Separator with N and S Dual-Doped Mesoporous Carbon Coating for Advanced Lithium-Sulfur Batteries. *ACS Appl Mater Interfaces* **2016,** *8* (23), 14586-95.

42. Zhu, J.; Yildirim, E.; Aly, K.; Shen, J.; Chen, C.; Lu, Y.; Jiang, M.; Kim, D.; Tonelli, A. E.; Pasquinelli, M. A.; Bradford, P. D.; Zhang, X., Hierarchical multi-component

nanofiber separators for lithium polysulfide capture in lithium–sulfur batteries: an experimental and molecular modeling study. *Journal of Materials Chemistry A* **2016,** *4* (35), 13572-13581.

43. Zhao, T.; Ye, Y.; Peng, X.; Divitini, G.; Kim, H.-K.; Lao, C.-Y.; Coxon, P. R.; Xi, K.; Liu, Y.; Ducati, C.; Chen, R.; Kumar, R. V., Advanced Lithium-Sulfur Batteries Enabled by a Bio-Inspired Polysulfide Adsorptive Brush. *Advanced Functional Materials* **2016,** *26* (46), 8418-8426.

44. Kong, W. B.; Yan, L. J.; Luo, Y. F.; Wang, D. T.; Jiang, K. L.; Li, Q. Q.; Fan, S. S.; Wang, J. P., Ultrathin MnO2/Graphene Oxide/Carbon Nanotube Interlayer as Efficient Polysulfide-Trapping Shield for High-Performance Li-S Batteries. *Advanced Functional Materials* **2017,** *27* (18).

45. Evers, S.; Yim, T.; Nazar, L. F., Understanding the Nature of Absorption/Adsorption in Nanoporous Polysulfide Sorbents for the Li–S Battery. *The Journal of Physical Chemistry C* **2012,** *116* (37), 19653-19658.

46. Zhou, H. C.; Long, J. R.; Yaghi, O. M., Introduction to Metal-Organic Frameworks. *Chem. Rev.* **2012,** *112* (2), 673-674.

47. Xia, W.; Mahmood, A.; Zou, R. Q.; Xu, Q., Metal-organic frameworks and their derived nanostructures for electrochemical energy storage and conversion. *Energy & Environmental Science* **2015,** *8* (7), 1837-1866.

48. Li, J. R.; Sculley, J.; Zhou, H. C., Metal-Organic Frameworks for Separations. *Chem. Rev.* **2012,** *112* (2), 869-932.

49. Lee, J.; Farha, O. K.; Roberts, J.; Scheidt, K. A.; Nguyen, S. T.; Hupp, J. T., Metal-organic framework materials as catalysts. *Chemical Society Reviews* **2009,** *38* (5), 1450-1459.

50. Kreno, L. E.; Leong, K.; Farha, O. K.; Allendorf, M.; Van Duyne, R. P.; Hupp, J. T., Metal-Organic Framework Materials as Chemical Sensors. *Chem. Rev.* **2012,** *112* (2), 1105-1125.

51. Zheng, Y.; Zheng, S.; Xue, H.; Pang, H., Metal–organic frameworks for lithium–sulfur batteries. *Journal of Materials Chemistry A* **2019,** *7* (8), 3469-3491.

52. Bai, S.; Liu, X.; Zhu, K.; Wu, S.; Zhou, H., Metal–organic framework-based separator for lithium–sulfur batteries. *Nature Energy* **2016,** *1* (7).

53. Bai, S.; Zhu, K.; Wu, S.; Wang, Y.; Yi, J.; Ishida, M.; Zhou, H., A long-life lithium–sulphur battery by integrating zinc–organic framework based separator. *Journal of Materials Chemistry A* **2016,** *4* (43), 16812-16817.

54. Guo, Y.; Sun, M.; Liang, H.; Ying, W.; Zeng, X.; Ying, Y.; Zhou, S.; Liang, C.; Lin, Z.; Peng, X., Blocking Polysulfides and Facilitating Lithium-Ion Transport: Polystyrene Sulfonate@HKUST-1 Membrane for Lithium-Sulfur Batteries. *ACS Appl Mater Interfaces* **2018,** *10* (36), 30451-30459.

55. Lee, D. H.; Ahn, J. H.; Park, M.-S.; Eftekhari, A.; Kim, D.-W., Metal-organic framework/carbon nanotube-coated polyethylene separator for improving the cycling performance of lithium-sulfur cells. *Electrochimica Acta* **2018,** *283*, 1291-1299.

56. Li, M.; Wan, Y.; Huang, J.-K.; Assen, A. H.; Hsiung, C.-E.; Jiang, H.; Han, Y.; Eddaoudi, M.; Lai, Z.; Ming, J.; Li, L.-J., Metal–Organic Framework-Based Separators for Enhancing Li–S Battery Stability: Mechanism of Mitigating Polysulfide Diffusion. *ACS Energy Letters* **2017,** *2* (10), 2362-2367.

57. Suriyakumar, S.; Kanagaraj, M.; Kathiresan, M.; Angulakshmi, N.; Thomas, S.; Stephan, A. M., Metal-organic frameworks based membrane as a permselective separator for lithium-sulfur batteries. *Electrochimica Acta* **2018,** *265*, 151-159.

58. Wu, F.; Zhao, S.; Chen, L.; Lu, Y.; Su, Y.; Jia, Y.; Bao, L.; Wang, J.; Chen, S.; Chen, R., Metal-organic frameworks composites threaded on the CNT knitted separator for suppressing the shuttle effect of lithium sulfur batteries. *Energy Storage Materials* **2018,** *14*, 383-391.

59. Tian, M.; Pei, F.; Yao, M.; Fu, Z.; Lin, L.; Wu, G.; Xu, G.; Kitagawa, H.; Fang, X., Ultrathin MOF nanosheet assembled highly oriented microporous membrane as an interlayer for lithium-sulfur batteries. *Energy Storage Materials* **2018**.

60. Zhao, K.; Liu, S.; Ye, G.; Gan, Q.; Zhou, Z.; He, Z., High-yield bottom-up synthesis of 2D metal–organic frameworks and their derived ultrathin carbon nanosheets for energy storage. *Journal of Materials Chemistry A* **2018,** *6* (5), 2166-2175.

61. Huang, L.; Zhang, X.; Han, Y.; Wang, Q.; Fang, Y.; Dong, S., In situ synthesis of ultrathin metal–organic framework nanosheets: a new method for 2D metal-based nanoporous carbon electrocatalysts. *Journal of Materials Chemistry A* **2017,** *5* (35), 18610-18617.

62. Zhao, M.; Wang, Y.; Ma, Q.; Huang, Y.; Zhang, X.; Ping, J.; Zhang, Z.; Lu, Q.; Yu, Y.; Xu, H.; Zhao, Y.; Zhang, H., Ultrathin 2D Metal-Organic Framework Nanosheets. *Adv Mater* **2015,** *27* (45), 7372-8.

63. Leng, Y., *Materials Characterization Introduction to Microscopic and Spectroscopic Methods*. Second ed.; Wiley-VCH: 2013.

64. Uo, M.; Wada, T.; Sugiyama, T., Applications of X-ray fluorescence analysis (XRF) to dental and medical specimens. *Japanese Dental Science Review* **2015,** *51* (1), 2-9.

65. John C. Vickerman, I. S. G., *Surface Analysis - The Principle Techniques*. Second ed.; 2009.

66. Yang, X.; Rogach, A. L., Electrochemical Techniques in Battery Research: A Tutorial for Nonelectrochemists. *Advanced Energy Materials* **2019**.

67. Liao, J.; Ye, Z., Nontrivial Effects of "Trivial" Parameters on the Performance of Lithium–Sulfur Batteries. *Batteries* **2018,** *4* (2), 22.

68. Liu, S.; Zhou, J.; Song, H., 2D Zn-Hexamine Coordination Frameworks and Their Derived N-Rich Porous Carbon Nanosheets for Ultrafast Sodium Storage. *Advanced Energy Materials* **2018,** *8* (22).

69. Dementjev, A. P.; de Graaf, A.; van de Sanden, M. C. M.; Maslakov, K. I.; Naumkin, A. V.; Serov, A. A., X-ray photoelectron spectroscopy reference data for identification of the C3N4 phase in carbon-nitrogen films. *Diam. Relat. Mat.* **2000,** *9* (11), 1904-1907.

70. Valvekens, P.; Jonckheere, D.; De Baerdemaeker, T.; Kubarev, A. V.; Vandichel, M.; Hemelsoet, K.; Waroquier, M.; Van Speybroeck, V.; Smolders, E.; Depla, D.; Roeffaers, M. B. J.; De Vos, D., Base catalytic activity of alkaline earth MOFs: a (micro)spectroscopic study of active site formation by the controlled transformation of structural anions. *Chem. Sci.* **2014,** *5* (11), 4517-4524.

71. Baltrusaitis, J.; Jayaweera, P. M.; Grassian, V. H., XPS study of nitrogen dioxide adsorption on metal oxide particle surfaces under different environmental conditions. *Phys Chem Chem Phys* **2009,** *11* (37), 8295-305.

72. Awan, S. U.; Hasanain, S. K.; Bertino, M. F.; Jaffari, G. H., Effects of substitutional Li on the ferromagnetic response of Li co-doped ZnO:Co nanoparticles. *Journal of Physics-Condensed Matter* **2013,** *25* (15).

73. Barchasz, C.; Molton, F.; Duboc, C.; Lepretre, J. C.; Patoux, S.; Alloin, F.,

Lithium/Sulfur Cell Discharge Mechanism: An Original Approach for Intermediate Species Identification. *Analytical Chemistry* **2012,** *84* (9), 3973-3980.

74. Pang, Q.; Kundu, D.; Cuisinier, M.; Nazar, L. F., Surface-enhanced redox chemistry of polysulphides on a metallic and polar host for lithium-sulphur batteries. *Nature Communications* **2014,** *5*.

75. Seh, Z. W.; Wang, H.; Hsu, P.-C.; Zhang, Q.; Li, W.; Zheng, G.; Yao, H.; Cui, Y., Facile synthesis of Li 2 S–polypyrrole composite structures for high-performance Li 2 S cathodes. *Energy & Environmental Science* **2014,** *7* (2), 672-676.

76. Hong, X.; Jin, J.; Wu, T.; Lu, Y.; Zhang, S.; Chen, C.; Wen, Z., A rGO–CNT aerogel covalently bonded with a nitrogen-rich polymer as a polysulfide adsorptive cathode for high sulfur loading lithium sulfur batteries. *Journal of Materials Chemistry A* **2017,** *5* (28), 14775-14782.

77. Zhao, M.; Huang, Y.; Peng, Y.; Huang, Z.; Ma, Q.; Zhang, H., Two-dimensional metal-organic framework nanosheets: synthesis and applications. *Chem Soc Rev* **2018,** *47* (16), 6267-6295.

78. Cuisinier, M.; Cabelguen, P.-E.; Evers, S.; He, G.; Kolbeck, M.; Garsuch, A.; Bolin, T.; Balasubramanian, M.; Nazar, L. F., Sulfur Speciation in Li–S Batteries Determined by Operando X-ray Absorption Spectroscopy. *The Journal of Physical Chemistry Letters* **2013,** *4* (19), 3227-3232.

79. Fan, C. Y.; Yuan, H. Y.; Li, H. H.; Wang, H. F.; Li, W. L.; Sun, H. Z.; Wu, X. L.; Zhang, J. P., The Effective Design of a Polysulfide-Trapped Separator at the Molecular Level for High Energy Density Li-S Batteries. *ACS Appl Mater Interfaces* **2016,** *8* (25), 16108-15.

80. Li, W.; Yao, H.; Yan, K.; Zheng, G.; Liang, Z.; Chiang, Y. M.; Cui, Y., The synergetic effect of lithium polysulfide and lithium nitrate to prevent lithium dendrite growth. *Nat Commun* **2015,** *6*, 7436.

81. Cheng, X.-B.; Yan, C.; Chen, X.; Guan, C.; Huang, J.-Q.; Peng, H.-J.; Zhang, R.; Yang, S.-T.; Zhang, Q., Implantable Solid Electrolyte Interphase in Lithium-Metal Batteries. *Chem* **2017,** *2* (2), 258-270.

82. Ryu, H. S.; Ahn, H. J.; Kim, K. W.; Ahn, J. H.; Lee, J. Y.; Cairns, E. J., Self-discharge of lithium-sulfur cells using stainless-steel current-collectors. *Journal of Power Sources* **2005,** *140* (2), 365-369.

83. Pei, A.; Zheng, G.; Shi, F.; Li, Y.; Cui, Y., Nanoscale Nucleation and Growth of Electrodeposited Lithium Metal. *Nano Lett* **2017,** *17* (2), 1132-1139.